

# **Radiation Hardness Assessment of MR sensors for Space Applications**

**Pedro Filipe Lança Alves**

Thesis to obtain the Master of Science Degree in

## **Engineering Physics**

Supervisor(s): Prof. Susana Isabel Pinheiro Cardoso de Freitas  
Prof. Patrícia Carla Serrano Gonçalves

### **Examination Committee**

Chairperson: Prof. Pedro Miguel Félix Brogueira  
Supervisor: Prof. Susana Isabel Pinheiro Cardoso de Freitas  
Member of the Committee: Dr. Ana Neves Vieira da Silva

**November 2017**



I would like to dedicate this work to Paula Matos from UTR's Group of CTN



# Acknowledgments

Before starting, I want to thank my parents for all of the motivation and monetary support which they have always given me. Without it, probably it would have been much more difficult to reach this level.

Also, I am very grateful for all of the support and countless hours of work done in cooperation with my two supervisors Professor Susana Freitas (INESC-MN) and Professor Patrícia Gonçalves (LIP). Thank you both for helping me in everything.

Secondly, I want to thank to all of the INESC-MN Team starting by the PhD students: Pedro Riberiro, Fernando, Marília, Joana (yes I know that you are not a PhD but for me you are at the same level), João Valadeiro, Miguel, Rita Soares, Tiago Monteiro, Mariana, for every help, support, (and components) that you all gave me. To the Senior Researchers: Ana, Karla, Diana, Vânia, and Lu Guang. A big thank to the engineers José Bernardo, Fernando and Virgínia Soares. To the Master's students and closest colleagues, Tiago, Serra, Débora, Tomás Riberiro, Tomás Martins, Jorge, Gupta, Nuno, Rui, Rafael, it was very good every time we spent together. I will never forget our amazing discussions during the lunchtime. Let's all hope that Débora changes her habits guys! Thanks to Natércia and Sandra! I also want to thank to the clean ladies and the securities which, every morning that I arrive or every night that I was going home, they were always nice and kind.

To the colleagues of LIP's Space Group, I know that little was the time that I spent there, still, I want to thank to Marco and Pedro. For the UTR's group of CTN, I want to thank to Paula Matos, Eduardo Alves, Luís Ferreira, Nuno Inácio, and Tiago, by turning possible the irradiation of the samples.

I also want to thank to all my other colleagues from Engineering Physics, to Professor Maria Gomes, to my friends from Jiu-Jitsu, from Almodôvar, from the residence, and especially, to my very good friend Marisa that supported me basically since from the first year of my academic course.

Lastly, I want to thank to two important persons: to Maria for the support that she has been given to me in everything and, also, for being a person for whom I have an extremely great connection and respect. Also, I could never forget my brother André, which was and always will be one of my biggest sources of motivation during all of my academic journey and for the rest of my life, even him without knowing it.

Thank you all.



## Resumo

O custo associado ao planeamento e realização de missões espaciais é extremamente elevado, daí ter começado a surgir a tendência da fabricação de naves espaciais de reduzidas dimensões. Miniaturização de componentes e naves espaciais e uso de componentes comerciais de uso genérico permitem obter missões mais viáveis. No entanto, toda poupança associada à construção um aparelho espacial baseado nestes componentes, leva a que muitas das vezes estes não sejam devidamente submetidos a importantes testes como, por exemplo, o de radiação. Esta falta de conhecimento leva a uma maior desconfiança em relação ao comportamento destes componentes quando sujeitos ao agressivo ambiente espacial. Nesse sentido, este projecto teve como propósito a investigação dos efeitos de radiação gama em sensores magnéticos para uso espacial, nomeadamente sensores magnetoresistivos. A implementação destes para uso espacial é bastante desejada uma vez que apresentam reduzidas dimensões, baixos consumos energéticos, e possuem uma vasta gama de aplicabilidade, o que os torna um forte candidato à substituição dos sensores de maiores dimensões anteriormente utilizados. A investigação dos efeitos da radiação nos sensores foi realizada através do estudo de parâmetros característicos como curva de transferência, estados de saturação, sinal magnetoresistivo, coercividade, desvio das curvas de transferência e sensibilidade. Três irradiações foram realizadas até uma dose ionizante total de 5 Mrad ter sido atingida. Durante as irradiações os sensores não foram alimentados. Dos resultados obtidos sugere-se que os sensores são resistentes a altas doses ionizantes uma vez que não se verificou nenhuma alteração significativa do comportamento dos mesmos.

**Keywords:** Magnetoresistência, Sensores magnetoresistivos, Irradiação gamma, Tolerância a radiação, Dose ionizante total



## **Abstract**

With the desire to turn planetary and space assessment more viable, concerns about mass and electrical consumption of a spacecraft are of extreme importance. Nowadays, a lot has been talked about the reduction of spacecraft by the implementation of commercial off the shelf components. The cons to the use of these are that, for many of the cases, it is not really known how these would react when subjected to radiation since they do not pass through any radiation test. The purpose of this project was to assess the gamma radiation effects on micro magnetic sensors based on magnetoresistive technology. The desire for the expansion and replacement of the previous bulkier and mature sensors by the magnetoresistive ones in space field has to do mainly with the fact that these have the necessary features in order to have more viable missions and also the possibility of a wide range of applicability. The assessment of radiation effects was done by inspecting the characteristic parameters of the magnetoresistive sensors like transfer curves, saturated states, output signals, coercivity, transfer curve offset and sensitivity before, during, and after the irradiations. Three steps of irradiation were done until to reach a total ionizing dose of 5 Mrad. During the irradiations, the sensors were under unbiased conditions. In the end, was observed that the sensors are rad hard, since any significant modification in their performance was observed for the total ionizing dose of  $\sim 5$  Mrad.

**Keywords:** Magnetoresistance, Magnetoresistive sensors, Gamma irradiation, Rad-hard , Total ionizing dose



# Contents

- 1 Introduction 1**
  - 1.1 Motivation . . . . . 1
  - 1.2 Goals . . . . . 3
  - 1.3 Dissertation outline . . . . . 3
  
- 2 Background 5**
  - 2.1 Magnetoresistance effect . . . . . 5
    - 2.1.1 Anisotropy magnetoresistance . . . . . 7
    - 2.1.2 Giant magnetoresistance and SV sensors . . . . . 8
    - 2.1.3 Tunnel magnetoresistance and MTJ sensors . . . . . 10
  - 2.2 MR sensors as current sensing device . . . . . 12
  - 2.3 Space radiation sources and its effects . . . . . 13
    - 2.3.1 Space radiation sources . . . . . 14
    - 2.3.2 Space radiation effects . . . . . 15
  - 2.4 Radiation hardness assurance . . . . . 18
  
- 3 State-of-the-art 21**
  - 3.1 Radiation damage in materials . . . . . 21
  - 3.2 Radiation effects on magnetoresistive sensors . . . . . 22
  
- 4 Sensors designs, fabrication process and characterisation methods 25**
  - 4.1 Current sensors based on TMR effect - proposed design . . . . . 26
  - 4.2 SVs and MgO-based MTJ sensors - features and designs . . . . . 27
  - 4.3 Current sensors micro and nanofabrication process, and sensors implementation . . . . . 28

4.3.1	Deposition of MTJ stack . . . . .	28
4.3.2	Deposition of MTJ stack with e.a. reversed relative to the 1 <sup>st</sup> one . . . . .	30
4.3.3	Bottom electrodes definition . . . . .	31
4.3.4	MTJ pillar definition . . . . .	32
4.3.5	Ru temperature sensor . . . . .	34
4.3.6	Top electrodes definition . . . . .	34
4.3.7	Vias . . . . .	35
4.3.8	Dicing . . . . .	36
4.3.9	Wire bonding . . . . .	36
4.4	Characterisation methods . . . . .	37
4.4.1	Magnetotransport characterisation . . . . .	37
4.4.2	Profilometer . . . . .	37
<b>5</b>	<b>Irradiation and measurement of magnetoresistive parameters</b>	<b>39</b>
5.1	Irradiation experiment . . . . .	39
5.2	Results and discussion . . . . .	41
5.2.1	Magneto-transport curves . . . . .	41
5.2.2	Saturated states . . . . .	43
5.2.3	MR signal and WB output difference . . . . .	45
5.2.4	Coercivity . . . . .	46
5.2.5	Transfer curve offset relative to zero field . . . . .	46
5.2.6	Sensitivity . . . . .	47
<b>6</b>	<b>Conclusions</b>	<b>49</b>
	<b>Bibliography</b>	<b>51</b>
<b>A</b>	<b>Run-sheet - Current sensors</b>	<b>55</b>
<b>B</b>	<b>Radiation test plan</b>	<b>69</b>

# List of Tables

2.1	Key features of sensors implementing MR effect. Adapted from: [6, 7] . . . . .	6
2.2	Main sources and characteristics of radiation near-Earth orbit. Adapt from: [22] . . . . .	15



# List of Figures

2.1	(a) AMR geometry and readout scheme. (b) Simplified physical picture of AMR effect. (left/right) The fact of $I$ being parallel/perpendicular to $M$ (and to $H$ ) leads to deformations (induced by spin-orbit interactions) on the electronic clouds of FM material. From these deformations, a higher/lower scattering cross-sections may result since the cyclotron motion of electrons (scattering centers) will be transversal/parallel to the current plane resulting in a higher/lower resistance. From: [6, 9] . . . . .	7
2.2	(left) Variation of $R$ in function of an applied magnetic field associated to a pure structure implementing GMR effect, i.e., where the two FM layers are able to rotate. (right) Physical picture of GMR effect in the light of the two current model. $\rho_{\uparrow}$ and $\rho_{\downarrow}$ are the resistivity of the majority and minority electron spins, respectively, associated with the electron transport through a pure GMR structure. From: [12] . . . . .	8
2.3	(left) Schematic of SV sensor. $\Theta_p$ and $\Theta_f$ are the orientation between the magnetisations of the pinned and free layer, respectively, relative to the layer plane. (right) Transfer curve for a SV sensor. From: [6, 15] . . . . .	10
2.4	Spin transport mechanism along TMR general structure when the two FMs $\mathbf{M}$ orientations are (left) parallel and (right) anti-parallel to each other. From: [17]. . . . .	11
2.5	Typical MTJ structures with SAF strategy for the enhancement of MR properties. (left/right) There is a bottom/top-pinned structure where the PL may be found under/above the oxide layer. From: [18]. . . . .	11
2.6	Full Wheatstone bridge composed of MR elements. Among the other bridges configurations, this is the one for which is obtained the higher output signal given by $V_{output} = V_{bias} \frac{\Delta R}{R}$ , where $R_1 = R_4 = R + \Delta R$ and $R_2 = R_3 = R - \Delta R$ . From: [19]. . . . .	12
2.7	Main sources of radiation found in space. From: NASA . . . . .	13
2.8	Cosmic Rays spectrum: flux of nuclei (particles per-energy-per-nucleus) vs kinetic energy per particle. From: [23] . . . . .	14
2.9	Scheme of ionizing radiation effects on energy band diagram of $\text{SiO}_2$ . Adapt from: [5]. . .	16
2.10	TRL diagram. From: NASA . . . . .	19

4.1	Current sensor autocad design. The full Wheatstone bridge is displayed in line. Each of the four sets of resistors are constituted by 136 MTJs connected in series. Software Autocad 2015 . . . . .	26
4.2	SV autocad design. Software: Autocad 2015 . . . . .	27
4.3	MgO-based MTJ autocad design. Software Autocad 2015 . . . . .	28
4.4	(top) SVG track and (bottom) Direct write laser. . . . .	29
4.5	(left) MTJ stack which was deposited. (right) Scheme of the ion beam system. . . . .	30
4.6	Stack deposition in a two step process in order to get the two reversed e.a.'s, identified by the red and green arrows. Adapt from: [6]. . . . .	31
4.7	(left) Resistor with 136 MTJs connected in series. (right) Single MTJ. Color scheme:(yellow) region where was deposited MTJ stacks, (green) bottom electrodes, (red) MTJ pillar, (cyan) top electrodes, and (blue) vias. . . . .	32
4.8	(left) Microscopic image of the pattern of the MTJ pillars. (right) Scheme of the stack structure that is expected to be transfered after the etching of the pillars. . . . .	33
4.9	(left) RF magnetron sputtering apparatus (UHV2 system). (right) RF magnetron sputtering scheme. From: [7] . . . . .	34
4.10	Nordiko 7000 modules scheme. From: [7] . . . . .	35
4.11	(top left) Wire bonding machine, and (bottom right) microscope view of the connections made by the needle when moved with a mouse to the desired regions. (top right) Chip-carrier with the implemented sensor. . . . .	36
4.12	(top) Setup 140 Oe apparatus used for sensors characterisations. (middle) Setup electrical scheme. (bottom right) Chip-carrier connector and (bottom left) pin board selector. . .	38
5.1	Co-60 decay scheme. Source: Hyperphysics . . . . .	39
5.2	Evolution of the transfer curves along the irradiation experiment of a MgO-based MTJ sensor (sample MTJ 2.2). The stack associated to the sensor are identified (from the bottom to the top) by the material of each layer followed by its thickness given in angstroms. 42	42
5.3	Evolution of the transfer curves along the irradiation experiment of (left) Wheatstone bridge with AlOx-based MTJs (sample WB 10), and (right) SV (sample SV 2.2) sensor. .	42

5.4	Evolution of the saturated states, parallel ( $R_p$ ) and anti-parallel ( $R_{ap}$ ) resistances for the MgO-based MTJs (un-irradiated MTJ, MTJ 2_2 and 2_3) along the irradiation stages. The band represented in each graph represents the interval where variations were observed. These intervals have in consideration the maximum absolute deviations relative to the mean value of $R_p$ and $R_{ap}$ , where, for the MgO-based MTJs, maximum deviations of $\sim 0,3$ and $\sim 0,8 \Omega$ were, respectively, obtained. . . . .	44
5.5	Evolution of the saturated states, parallel ( $R_p$ ) and anti-parallel ( $R_{ap}$ ) resistances for the SVs (un-irradiated SV, SV 2_1 and 2_3) along the irradiation stages. The band represented in each graph represents the interval where variations were observed. These intervals were considered to be the maximum absolute deviation relative to the mean value of each sample. For the SVs, the intervals where variations are observed, are associated to maximum absolute deviations of $\sim 2$ and $\sim 1,5 \Omega$ relative to $R_p$ and $R_{ap}$ mean values, respectively. . . . .	44
5.6	Evolution of the saturated voltages, $V_{min}$ and $V_{max}$ , for the WBs (un-irradiated WB, WB 10 and 13) along the irradiation stages. For the WBs the variations of the irradiated were considered insignificant (one order below) when compared with the ones verified for the un-irradiated sensor $\sim 6$ mV for the $V_{max}$ and $V_{min}$ . . . . .	44
5.7	Evolution of the MR signal associated to the MgO-based MTJs along the irradiation stages. The bands represented the interval where the variations occurred. For this case, these intervals bands are associated to a maximum absolute deviations close to $\sim 1,1 \%$ . . . . .	45
5.8	Evolution of the MR signal for the SVs along the irradiation stages. For the SVs the intervals where variations were observed, are associated to maximum absolute deviations close to $0,1 \%$ . . . . .	45
5.9	Evolution of the output signal, $\Delta V_0 = V_{max} - V_{min}$ , for the WBs along the irradiation stages. . . . .	46
5.10	Coercivity evolution for the WBs (un-irradiated WB, WB 1, 10 and 13) along the irradiation stages. . . . .	46
5.11	Evolution of the transfer curve offset for (left) MgO-based MTJs, (middle) SVs, and (right) WBs along the irradiation stages. . . . .	47
5.12	Evolution of the sensitivity of the MgO-based MTJs along the irradiation stages. . . . .	47
5.13	Evolution of the sensitivity of the SVs along the irradiation stages. . . . .	47
5.14	Evolution of the sensitivities of the WBs along the irradiation stages. . . . .	48



# Nomenclature

## Physical quantities

$\rho$	Resistivity
H	Applied magnetic field
I	Electrical current
M	Magnetisation
R	Electrical resistance
T	Temperature

## Acronyms

AFM	Anti-ferromagnetic
AMR	Anisotropic magnetoresistance
COTS	Commercial-off-the-shelf
DD	Displacement damage
e.a.	Easy axis
FM	Ferromagnetic
GCR	Galactic cosmic ray
GMR	Giant magnetoresistance
MR	Magnetoresistance/magnetoresistive
MTJ	Magnetic tunnel junction
SPE	Solar particle event
SV	Spinvalve
TID	Total ionizing dose
TMR	Tunnel magnetoresistance

WB Wheatstone bridge





# Chapter 1

## Introduction

### 1.1 Motivation

There is still a lot of mystery about the cosmos to be unveiled. The Human being is, probably, the most curious creature in the universe. It is this intrinsic Human desire that has allowed the evolution of Mankind. Nowadays, society is being driven through a road which will get us to a state of readiness in order to take the next big step for Humanity, the “steepening” of another Planet. Since it was agreed to start to plan a manned trip to Mars, society started, again, to be agitated and encouraged to help this to happen in every possible way. From my point of view, I think this is a good attitude because it just gives us a higher probability of achieving success since more and more people are making an effort in the same direction. I think, also, that this will bring every nation and people close together. Meanwhile, we still have a lot of social issues to deal within our Home before going to “conquer” another planet.

So, now let me to put apart this my Humanistic point of view and let's talk about some important key points related with the development of successful space missions. For a manned Mars mission to be successful we must ensure that astronauts arrive alive and healthy at Mars's soil, and then return safely to the Earth. As we might know, the accomplishment of any space mission depends a lot on its budget. For a manned mission, I do not think that this will be a problem since there are lives involved. On the other hand, for un-manned missions, since cost plays a huge role on its execution, new and more viable strategies are required in order to ensure the high quality space research combined with a lower price. As we have been hearing a lot, a possible strategy for developing more efficient missions is through the miniaturization of spacecrafts and the implementation of high quality commercial off-the-shelf (COTS) components [1]. These components are known for being very cheap for the relative good quality that they present. Nevertheless, one of the counterparts of using these type of components is due to the fact that there is still little information about their tolerance to the radiation found in space environment. Nowadays it is being verified that many companies do not worry about if a component is rad hard or not, because qualifying them it would be expensive. So, the typical all-weather satellite, where practically

all of their components are resistant to extreme conditions, is starting to disappear. Since COTS are smaller and cheaper, companies are designing satellites with these in order to be able to launch as many as possible into space ensuring that some of them will work.

Since the end of the 60's beginning of 70's, we have been to observe further and further reductions of the size of components. The invention of the laser and the evolution of specialized technologies were some of the responsible for the development and enhancement of micro and nano fabrication techniques, allowing then the achievement of micro components. One of the main goals of miniaturisation is to reduce the final price of a device keeping its good quality and performance for research and society purposes. So, miniaturisation plays an important role in planning a space mission, since a bigger portion of its budget is related to the mass and power consumption associated with all spacecraft's apparatus. A portion of that mass is associated with the spacecraft's shielding, which has a protection function against the intense radiation found in space environment. Dealing with the mass needed for shielding it is a challenge, and some important points must be carefully treated. First, the mass must be very well considered since it can easily turn a possible mission in an impossible one if the associated budget is surpassed. Secondly (and somehow connected with the first aspect), the type and amount of material used for the shielding must be very well pondered in order to try to avoid the creation of another piece of "junk" floating in space. So we may have here a trade-off between the mass needed to maintain the functionality of a device and its associated costs. Meanwhile, some other new strategies that may allow a better and viable shielding like, for example, the production of mini-magnetospheres around a body are not totally excluded as Bamford et al. (2012) [2] shown.

Apart from turning space missions more viable, the use of miniaturised components may also contribute to the increase of the lifetime of an experiment, as also may allow a more reliable understanding of it. The former results from the possibility of having much more components, with smaller sizes, doing the same function instead of having a few bigger ones (typically bulkier but reliable technology due to its high mature level), where if one of these fails it may compromise an experiment. The same would not happen in the case where we have a lot of them, which basically would work as an assurance of functionality. The latter aspect has to do with the higher amount of collected data from an experiment, since more devices would mean higher amounts of data.

For instance, it is easy to understand that bulky components may have higher radiation tolerance, i.e., they are less susceptible to failures induced by radiation due to higher attenuation by the material, compared with miniaturised ones. For devices of the same type, different bias conditions and/or doses of radiation may lead to different responses. So we get kind of unpredictable behaviour on what might happen when devices are hit by cosmic radiation. This is why assessment of radiation hardening is not an easy task to deal with, and even less when we wish to assess radiation tolerance of relatively novel (at least for space applications) nano and micro magnetic components as, for example, the magnetoresistive sensors. These sensors are quite known for their wide range of applicability here on the ground. In terms of using them in space, there are already ongoing missions, like the Mars Rovers "Spirit", "Opportunity", and "Curiosity", implementing them in altitude and attitude positioning, and current measurement

systems, as mentioned by Slatter (2015) [3]. Although, for many of space applications, some of the bulky magnetic sensors still remain as a preferential option, e.g., the mature fluxgate. This has to do mainly with the necessity for more information about radiation tolerance and its effects in magnetoresistance technology, as also the need of improvements in their performance, for example, lower detectivities are needed for a magnetometer. Yet, it is expected that in a close future this technology, eventually, will start to replace the antique magnetic sensors currently used.

## **1.2 Goals**

As we already understood, the qualification process is a major factor in order to determine if a device is suitable or not for space applications. During space-flight qualification, components are submitted to different type of tests, and irradiation test is one of them. Through this test, it is possible to have some feedback about on whether or not the evaluated devices will perform well under the space harsh environment.

So, in this project, I focused on the evaluation of the long-term effect of space radiations in magnetoresistive sensors, without front end technology, in order to know their tolerance to radiation. From previous works [4, 5], proves were already shown that in principle magnetoresistive sensors present a good level of radiation tolerance. Nevertheless, due to the high randomness associated with the radiation-induced effects which a material may suffer, is fundamental to have more data to better support these evidence for these type of technology. And here is where this project enters which, basically, has the goal to analyse the behaviour of three different magnetoresistive sensors like spin-valves and AlOx and MgO based magnetic tunnel junctions, through the inspection of their main parameters, when submitted to ionizing radiation resulting on the deposit of energy on the sensors (that translates in ionizing dose).

## **1.3 Dissertation outline**

Before going to the experimental part of the project, in Chapter 2, I will begin with a brief review of the main concepts needed in order to get a better understanding of it. In Chapter 3, it is given an insight of the work, closely related to my project's theme, already done. In Chapter 4, aspects related to the sensors fabrication, sensors design, implementation, and characterisation methods are presented. Chapter 5 presents the description of the experiment itself and the results obtained from it. In Chapter 6, I finalize with some conclusions.



# Chapter 2

## Background

Here in this chapter is where I try to make the first connection between spintronics-based components (components governed by charge and spin mechanisms) and space radiation. In order to do that, I first start to briefly explain some of the main points associated with spintronics, for example, what is the magnetoresistive effect employed by thin film materials, what are the mechanisms behind it, and which sensors may implement it. The magnetic parameters which characterise each type of sensor will also be mentioned. Two possible applications of these sensors are explored. After this has been done, comes the second theme, where I start to characterise the space radiation environment by telling what are the main sources and associated types of radiation found in space. Then, we will see what are the effects associated to the interaction of the radiation with devices.

### 2.1 Magnetoresistance effect

Magnetoresistance (MR) effect may be defined as the change of an electrical resistance, when a current flow through a material, due to the application of a magnetic field,  $R = f(H)$ . It is possible to categorise MR phenomenon according to the mechanism behind its origin. Although the existence of a variety of mechanisms, according to the different type of materials where MR effect may surge, there is one which is common to all of the materials (macroscopic property) - "ordinary" magnetoresistance (OMR) - which is only dependent on the amplitude and direction of the applied magnetic field. OMR comes as consequence of a well-known phenomenon called "ordinary" Hall effect. In Hall effect, we have that the application of a magnetic field orthogonal to an electric current ( $I$ ) will induce the appearance of a perpendicular electric field (due to the Hall potential that surge also perpendicular to  $I$ ) which will pull the charge carriers apart from the current direction. This deviation will result in an increase of the resistance throughout the material.

Nevertheless, the phenomena that will be explored come from microscopic mechanisms which associated to an "extraordinary" MR effect. Extraordinary because higher variations of resistance compara-

tively with OMR are observed, and that is why they are considered the more relevant ones in terms of the development of devices and practical applications. Here, I only will briefly explain the three main categories: anisotropic magnetoresistance (AMR), giant magnetoresistance (GMR), and tunnel magnetoresistance (TMR). One common parameter to all of MR mechanisms is the MR signal, which may be quantified as the maximum variation of the resistance, and can be represented in the following ratio form:

$$MR(\%) = \frac{R_{max} - R_{min}}{R_{min}} \times 100. \quad (2.1)$$

Typically, a magnetic material can present magnetic anisotropy, i.e., magnetic moments may tend to align with specific directions. An easy axis (e.a.) may be define as the preferential directions under which magnetic moments have a tendency to align. This orientation, it is considered the one for which a smaller magnetic field is needed (i.e., with minimal state of energy) in order to align the moments. Oppositely, a hard axis (h.a.) corresponds to a maximum energy state. Magnetic anisotropy origin is related to sample geometry (shape anisotropy), the atomic structure of a crystal (magnetocrystalline anisotropy), stress (magnetoelastic anisotropy), and interface interaction between pairs of different type of materials (exchange bias anisotropy).

It is possible to induce an anisotropy (and so define and e.a.) in materials exhibiting magnetic isotropy transforming their weak long-range ordering in a stronger one. This can be done by the application of a magnetic field during the deposition process of materials, and/or due to a magnetic annealing treatment of the material, and also by playing with the combination of specific materials and their thicknesses (resulting, for example, in an exchange bias coupling between interfaces). This may be important since, in order to have a suitable magnetic sensor, it is commonly required that some part of the sensor may be seen as a stable reference. So if a specific material is not properly magnetised, the final device may not present the desired properties.

Depending on the type and requirements of an application, one of the three MR's mechanisms mentioned above is typically among the elected choice. On the Table 2.1 it is summarized the sensor's main feature employed by the different kind of MR mechanisms. MR effect has been extensively used for a while in magnetic recording, magnetic field sensors, non-volatile memories, among many others applications.

Table 2.1: Key features of sensors implementing MR effect. Adapted from: [6, 7]

	AMR	GMR - Spinvalves (SV)	TMR - Magnetic tunnel junctions (MTJ)
<b>Physical principle</b>	Anisotropic MR	Giant MR	Spin dependent tunneling
<b>Thin film structure</b>	Simple Buffer/free/cap	Multilayers composed by diverse materials Buffer/pinning/reference/spacer/free/cap	Complex multilayers composed by diverse materials Buffer/pinning/reference/barrier/free/cap 50% (Al <sub>2</sub> O <sub>3</sub> , amorphous barrier) 300% (MgO crystalline barrier)
<b>MR ratio (%)</b>	2 - 6	6 - 20	up to 360 °C
<b>Thermal stability</b>	up to 250 °C	up to 320 °C	up to 360 °C
<b>Sensor linear range (Oe)</b>	1 - 100	10 - 50	20 - 100
<b>Magnetic anneal treatment (°C)</b>	not required	~ 250	~ 350
<b>Electrostatic discharge protection (robustness)</b>	very good	good	fair
<b>Materials cost</b>	cheap	expensive	expensive

## 2.1.1 Anisotropy magnetoresistance

In 1856, William Thomson, mostly known as Lord Kelvin, discovered a special property of magnetic materials called anisotropic magnetoresistance (AMR). Through the inspection of simple material geometries as the one presented in Figure 2.1 (a), he observed [8] that the electrical resistance of iron (Fe) and nickel (Ni) changed accordingly to the direction of the magnetisation ( $\mathbf{M}$ ) when submitted to an external magnetic field. Kelvin had seen that for a longitudinal/transverse magnetisation in relation to a current passing through Ni and Fe, a higher/lower resistance state was obtained. This change of states is associated with a deformation of electronic orbits which increase or decrease scattering cross-section depending on the orientation of  $\mathbf{M}$ . This was the first evidence of a microscopic magnetoresistance effect on a magnetic material.

For temperatures  $T$  well below Curie temperatures  $T_c$  ( $T < T_c$ ), materials like Fe (1043 K), Ni (627 K), and Co (1400 K), may present ferromagnetic properties, i.e., the magnetic moments of unpaired electron spins tend to be aligned spontaneously along specific directions (magnetocrystalline anisotropy), forming then, magnetic domains characterised by a long-range ordering. For temperatures above  $T_c$ , long-range ordering vanishes. In these materials, resistivity  $\rho$  varies with the relative orientation between the spontaneous magnetisation and the electric current flowing through it, when  $H$  is applied, as it is represented in Figure 2.1 (b). AMR effect results as a consequence of anisotropic mixing of spin-up and down in the material conduction's subbands provoked by spin-orbit interactions.

For this specific mechanism, and similar to (2.1), McGuire and Potter (1985) [10] shown that AMR ratio may be quantified as

$$AMR = \frac{\rho_{\parallel} - \rho_{\perp}}{\rho_{av}}, \quad (2.2)$$

where  $\rho_{\parallel}$  is typically the maximal resistivity, during the application of  $H$ , and characterise the case where

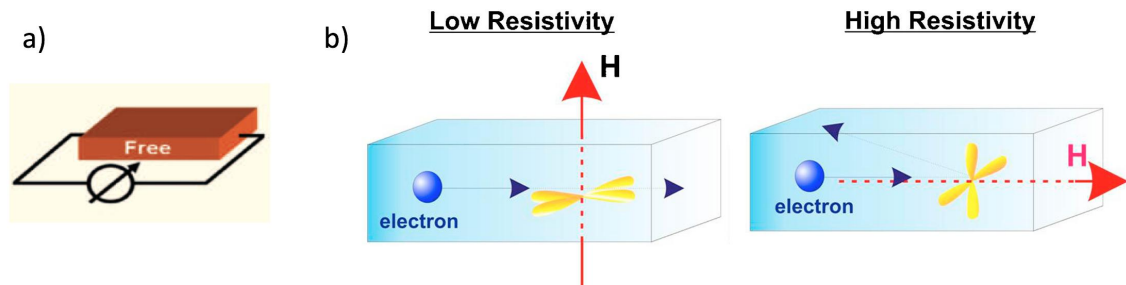


Figure 2.1: (a) AMR geometry and readout scheme. (b) Simplified physical picture of AMR effect. (left/right) The fact of  $I$  being parallel/perpendicular to  $M$  (and to  $H$ ) leads to deformations (induced by spin-orbit interactions) on the electronic clouds of FM material. From these deformations, a higher/lower scattering cross-sections may result since the cyclotron motion of electrons (scattering centers) will be transversal/parallel to the current plane resulting in a higher/lower resistance. From: [6, 9]

$\mathbf{M}$  is parallel  $\parallel$  to  $\mathbf{l}$  in a FM conductor,  $\rho_{\perp}$  is the minimum resistivity associated to the case where  $\mathbf{M}$  is perpendicular  $\perp$  to  $\mathbf{l}$ , and  $\rho_{av} = (\rho_{\parallel} + 2\rho_{\perp})/3$  is the average resistivity which may represent approximately the resistivity at zero field.

Sensors based on this effect present a low noise level and a low signal as we can see in Table 2.1 (AMR  $\sim 2 - 6\%$ ), among other features. This technology is already well mature and used in space applications [1]. Sensors based on this effect like the Planar Hall effect (PHE) sensor have been explored and used as space magnetometers since a while [11].

## 2.1.2 Giant magnetoresistance and SV sensors

### • Giant magnetoresistance

With the industrial evolution and advances on thin films deposition techniques, more ambitious requirements and better MR device performances started to be demanded. This led researchers to investigate ways of getting higher sensitivities  $\Delta R/\Delta H_{linear}$ , since AMR's mechanism just was able to provide a lower MR signal. From the exploration of engineered multilayers structures composed by specific materials, Baibich et. al. (1988) [13] discovered a new kind of effect was an "anomalous" MR signal was obtained. This was verified in a sandwich system composed of two FM transition metals, separated by a non-magnetic material (typically Cr, Cu, or Ru), exhibiting antiferromagnetic coupling (at zero field,  $H = 0$ ). From Figure 2.2 is possible to observe that under the application of an external magnetic field ( $H \neq 0$ ), AF coupling may be replaced by FM coupling as the magnetisation of one of the two FM layers rotates. GMR's amplitude depends greatly on the interaction between FM and non-magnetic materials, as also on their thickness.

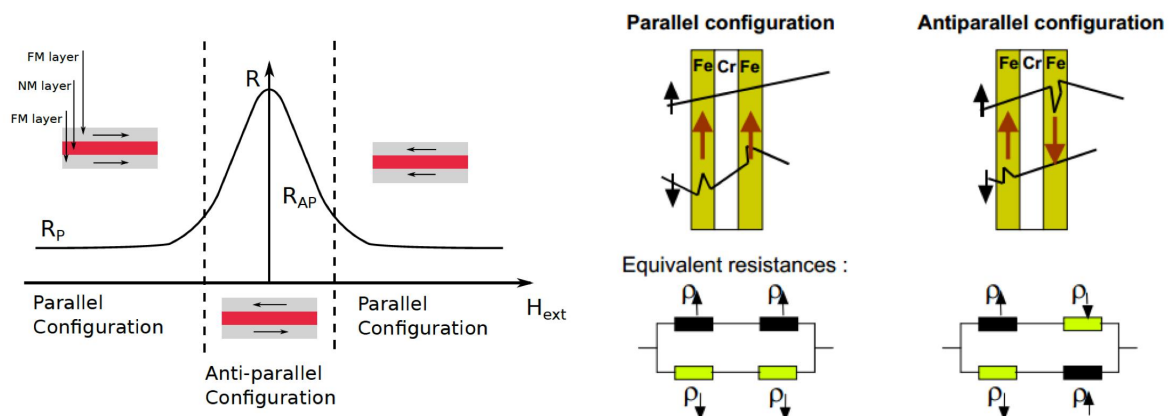


Figure 2.2: (left) Variation of  $R$  in function of an applied magnetic field associated to a pure structure implementing GMR effect, i.e., where the two FM layers are able to rotate. (right) Physical picture of GMR effect in the light of the two current model.  $\rho_{\uparrow}$  and  $\rho_{\downarrow}$  are the resistivity of the majority and minority electron spins, respectively, associated with the electron transport through a pure GMR structure. From: [12]

This effect may be explained in the light of the two current model where two spaced FM layers are considered to be the parallel of two sets of resistors as it is represented in Figure 2.2 (left). This model is valid since FM transition metals have a weak spin-orbit coupling and because magnon scattering effects may be negligible (at low temperatures), as well as other scattering events. In this model, each resistor represents the flow of electrons with spin parallel ( $\uparrow$  - majority spin) or anti-parallel ( $\downarrow$  - minority spin) to the magnetisations, through the FM layers and their interfaces. From the first situation (spins  $\parallel$  to  $\mathbf{M}$ ) we have a ferromagnetic coupling between the two metals which translates into a lower resistance state ( $R_p$ ), while for the other case (spins anti-parallel to  $\mathbf{M}$ ) there is an antiferromagnetic coupling (at zero field, which depends on the spacer thickness as Baibich et al. (1988) [13] have shown). This type of coupling is associated to stronger scattering effects on the non-magnetic/FM interfaces contributing to a higher resistance state ( $R_{ap}$ ). So, GMR effect is associated to the diffusive process of two types of electron's spins, where the majority spin is less scattered than minority spin - electron spin-dependent scattering process - as it is depicted by the two current model in Figure 2.2 (right).

Contrarily to AMR, GMR's mechanism does not have to do with relative orientations between  $I$  and  $M$ , but yes with the orientation of magnetisations between the two separated FM layers. Conjugating with this, there is also the existence of an asymmetry in the spin density of states in band structure of FM metals (due to overlapping of the usual incomplete 3d bands of the electronic structures of the materials) where electrons with a specific spin may suffer more or less scattering according if with the existence of more or less available spin states at Fermi energy. More available states mean less scattering, and vice-versa.

Nevertheless, for this mechanism in its pure form, parallel and anti-parallel magnetisations states are not so easy to control since the two FL layers are free to rotate which translates into an oscillatory coupling as we saw in Figure 2.2 (left). This makes pure GMR effect undesired in terms of, for example, sensing magnetic fields or magnetoresistive reading heads applications since small and symmetrical MR signals would be obtained during the application of a magnetic field, due to the fact, of not having a fixed magnetised orientation. In the nineties, with the objective to surpass this challenge, IBM explored a new system - spinvalve - where it became possible to stabilize the two saturated states (parallel and anti-parallel resistance states) by pinning a FM layer (fixing its magnetisation orientation).

- **Spin valves**

Spin valve (SV) is a simple GMR-based system and, so, its active region can be simply composed of a FM / non-magnetic conductor / FM structure plus one AF layer. A typical design of SV sensor is shown in Figure 2.3 (left). The presence of the AF layer adjacent to a FM layer will be the main difference between this system and a "pure" GMR one where, instead of having an oscillatory coupling, a reference direction of magnetisation will be defined in one of the FM layers (pinned layer - PL) by exchange bias coupling with the AF layer, while the magnetisation of the other FM will be free to rotate during the presence of an external magnetic field (free layer - FL). In these case, the reference layer (RL) is the same as the pinned one. So, for systems like this, it becomes possible to obtain two different saturated resistance states, as it is shown in Figure 2.3 (right). Again, these are associated to  $R_{ap}$  and  $R_p$ , but

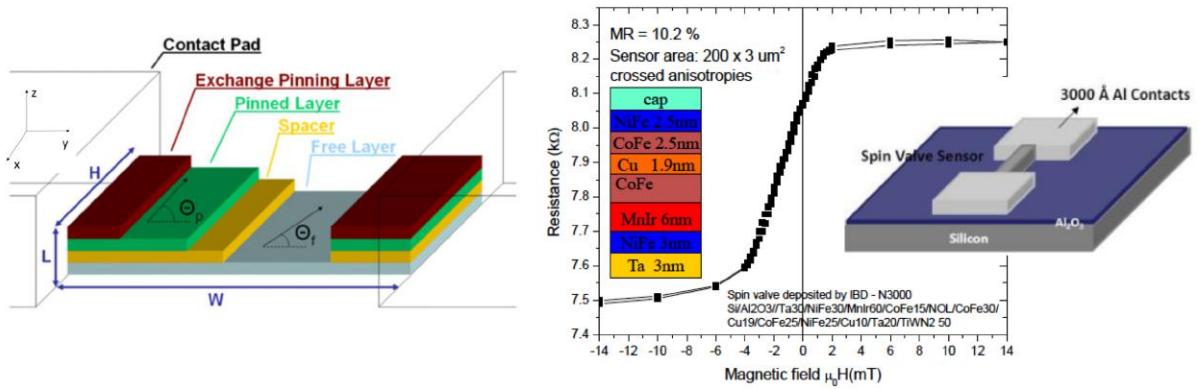


Figure 2.3: (left) Schematic of SV sensor.  $\Theta_p$  and  $\Theta_f$  are the orientation between the magnetisations of the pinned and free layer, respectively, relative to the layer plane. (right) Transfer curve for a SV sensor. From: [6, 15]

now without verifying the oscillatory coupling under small fields values (larger field values are needed in order to rotate the PL - increase of the exchange bias field). For these systems, a higher MR signal at the same field regime which translates into an improvement in device sensitivity. A good review about GMR effect and SV may be found at [14].

### 2.1.3 Tunnel magnetoresistance and MTJ sensors

- **Tunnel magnetoresistance**

Tunnel magnetoresistance (TMR) is the last MR mechanism mentioned here and is the one from which higher MR signals are possible to be reached (Table 2.1 at page 7). TMR is considered a (non-diffusive) spin-dependent mechanism [16], where electrons cross two FM layers (perpendicular to the plane) separated by an insulator one (instead of a non-magnetic as in the case of GMR effect) through which the FM layers are weakly ferromagnetically coupled. When a voltage is applied between two electrodes separated by the insulator, spin  $\uparrow$  and  $\downarrow$  electrons from the FM layer will occupy the available equivalent spins states in the other FM layer after to tunnel the barrier. During this process spin is conserved.

The tunnel effect electron spin dependency has to do with the existence of an asymmetry between the densities of states (DOS) associated to spin  $\uparrow$  and  $\downarrow$  close to the Fermi level of the FM layers, as it is represented in Figure 2.4. As a consequence of this asymmetry, we may have, between the two FM layers, a parallel or anti-parallel  $\mathbf{M}$  orientation. These two relative orientations are associated with a lower and higher resistance states, respectively. The lower/higher resistance is associated with the fact that the two electrons spins have a lower/higher probability to tunnel the barrier into states with similar/different spin density of states.

- **Magnetic tunnel junctions**

TMR effect based sensors are denominated as magnetic tunnel junctions (MTJs) and present a very similar structure as the SVs, being the presence of the insulating barrier the main difference, and related

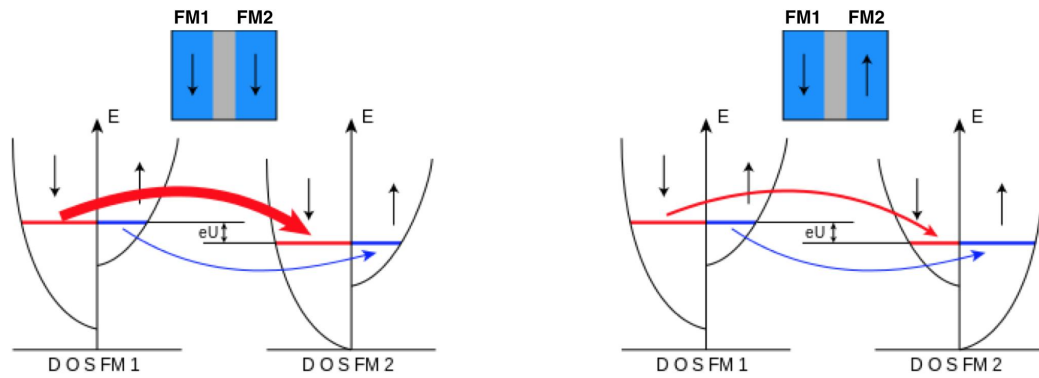


Figure 2.4: Spin transport mechanism along TMR general structure when the two FMs  $\mathbf{M}$  orientations are (left) parallel and (right) anti-parallel to each other. From: [17].

with this, the fact that current flows perpendicular to the plane (CPP).

A MTJ sensor may be formed by the following thin film structures, as presented in Figure 2.5:

- Buffer/seed - is a combination of layers (composed, e.g., of Ta and Ru) which has the purpose to enhance electrical properties and also to ensure proper crystallographic grow of the upper layers;
- FL - this a FM layer (CoFe, CoFeB, Fe, NiFe) where the free rotation of its magnetisation will be associated to the sensing of an external magnetic field;
- Insulator - may be composed by AlOx (aluminum oxide) or MgO (Magnesium Oxide) with thicknesses between 5 - 20 Å. Depending on application's requirements it may be used AlOx or MgO barriers, among others. Typically, for magnetic sensors with AlOx barriers, lower MR ratios are obtained (~ 50 %) comparatively when MgO is used (up to 300 %). Nevertheless, the use of AlOx barriers has associated several advantages: easier fabrication process as their quality only depends on how much non-conductive they can be (no need for proper crystallographic control), and the possibility of using more materials as electrodes. For the MgO barriers, in order to have the most benefit from the underlie properties of coherent tunnelling process, a specific crystallographic

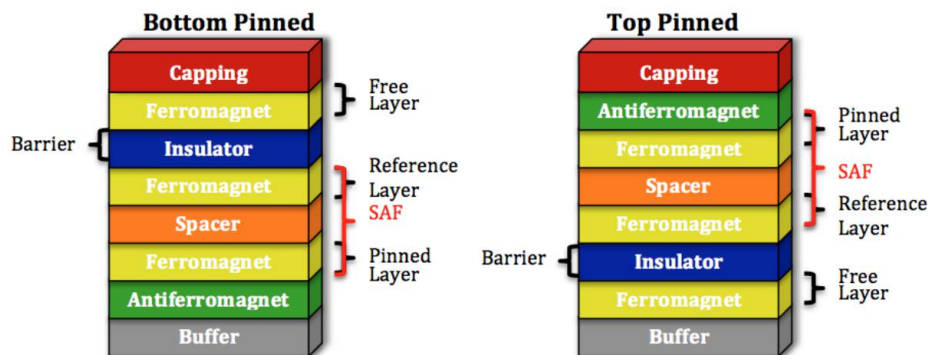


Figure 2.5: Typical MTJ structures with SAF strategy for the enhancement of MR properties. (left/right) There is a bottom/top-pinned structure where the PL may be found under/above the oxide layer. From: [18].

orientation is necessary and so during fabrication process is require more control of deposition and annealing parameters, and a wiser choice of electrode materials;

- SAF (synthetic antiferromagnetic) - this is composed of two FM layers (CoFe, CoFeB, Fe, or NiFe) separated by a spacer (e.g. Ru) with thickness (thinner than 10 Å) tuned in order to achieve AF coupling between the two FM layers, being one of them pinned by exchange bias interaction with an antiferromagnetic material. With this strategy the FM layer adjacent to the insulator will have a well defined magnetisation orientation (RL) even at higher fields ( $\sim$  kOe). Apart from this improvement in magnetic stability associated to the increase of the exchange bias field, SAF strategy still allows the reduction of the magnetostatic coupling between the reference and sensing layer (due to the characteristic null net magnetisation of SAF's structure at low fields), and an improvement of thermal stability;
- Cap - may be formed by the overlapping of Ru with Ta. This combination provides protection against oxidation and corrosion of the layers below.

Now that the main MR mechanisms, as well as the type of sensors implementing them, were presented, let's see how these may be applied in one type of application like a current sensing device.

## 2.2 MR sensors as current sensing device

Nowadays, having high precision current sensing devices capable of estimating the power consumption of an electrical system is of extreme importance. Typical requirements of current sensing applications are linearity, large output signals, null offset, and stable output values under a wide range of temperatures. Gathering these with the desired of having small, low power, and cheaper devices, makes the choice of using a MR technology-based current sensing device a very strong one.

For every metal wire driven by an electrical current, a magnetic field may be generated. The relation

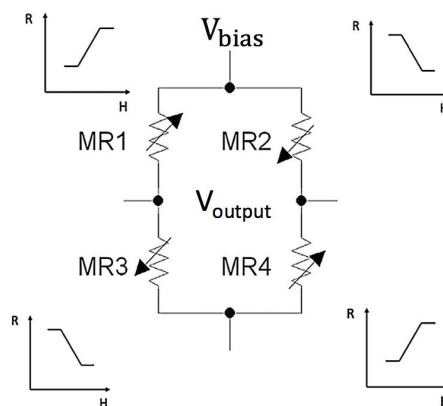


Figure 2.6: Full Wheatstone bridge composed of MR elements. Among the other bridges configurations, this is the one for which is obtained the higher output signal given by  $V_{output} = V_{bias} \frac{\Delta R}{R}$ , where  $R_1 = R_4 = R + \Delta R$  and  $R_2 = R_3 = R - \Delta R$ . From: [19].

between  $I$  and  $B$  is given by the Biot-Savart Law. So, by putting a MR sensor close to a current wire, the magnetic field produced by this current may start to be sensed by it, resulting in a specific sensor output. Then, with a previous calibration, it is possible to use these sensors as a (contactless) current sensing devices.

Using resistors composed of series of MTJs in a full Wheatstone bridge configuration, presented in Figure 2.6, is one of the best options for the implementation of a current sensor [20], since it satisfies practically all of the requirements before mentioned.

So, if we wish to implement these or other any type of device in a spacecraft, a previous very good knowledge about the space radiation environment and their effects on MR technology is need.

## 2.3 Space radiation sources and its effects

Here, on the ground, due to the atmosphere and our natural magnetic shield, called magnetosphere, we are protected against the dangerous electromagnetic (e.g. gamma rays) and particles radiation (e.g. protons, alpha particles) from the cosmos. Depending on our altitude and latitude, our protection may be more or less efficient. Higher altitudes mean less protection since, at high atmosphere, there are fewer particles to attenuate cosmic radiations. This is why astronauts and components need extra protection when travel to space (in interplanetary space there are only  $\sim 10$  particles per  $\text{cm}^3$ ).

As I already mentioned, the importance of this project comes from the necessity to get a better understanding of radiation effects on MR sensors and their radioresistance. Depending on different factors associated with radiation-matter interactions, a magnetic device may, whether or not, present radiation-induced defects which may possibly provoke degradation of its performance and of the device itself. So, it is very important to have a very good knowledge about the space radiation environment and its effects in order to mitigate radiation issues on Humans and components.

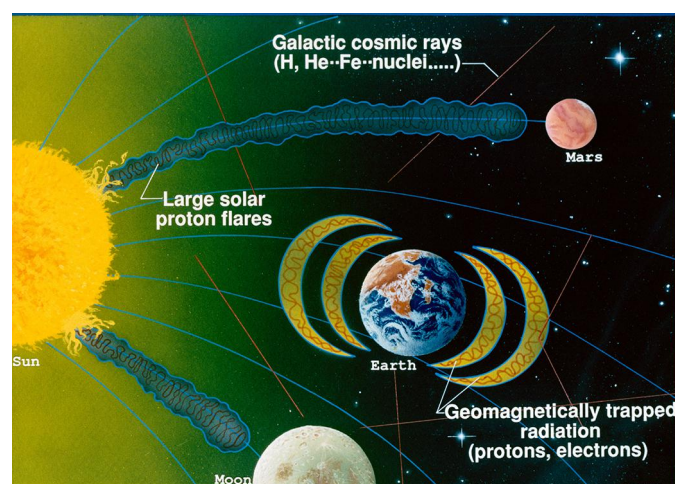


Figure 2.7: Main sources of radiation found in space. From: NASA

Benton (2001) [21] and Xanthos et al. (2012) [22] published two very good review articles where the characterisation, as well as the modeling of space radiation environment, are made. From Figure 2.7 we can distinguish the three main sources of space radiation: Cosmic Galactic Rays (CGRs), Solar Particle Events (SPEs), and charged particles trapped in magnetic fields.

### 2.3.1 Space radiation sources

- **Cosmic galactic rays**

Many believed that CGRs come from supernovae (and Active Galactic Nucleus), since from the analysis of their spectrum presented in the Figure 2.8, is possible to identify a decrease of nuclei flux as their atomic number  $Z$  increases. It is thought that this reduction as to do with the decrease in the abundance of elements within a star as it evolves, where, the lightest elements will fuse in heavier ones when burnt, and so the smaller fluxes associated to nuclei with higher  $Z$ .

GCRs are mainly composed of charged particles where 98% are protons and heavier ions. The remain 2% are electrons and positrons. GCRs are very well known for having the highest energies in the cosmos. Within our solar system, they can have some tens of MeV up to  $10^{12}$  MeV. Comparatively with the other two sources, GCRs are also known by having the lowest flux of particles, as showed in the Table 2.2.

One important aspect of GCRs fluxes is that they are modulated by solar activity, where a rapid decrease

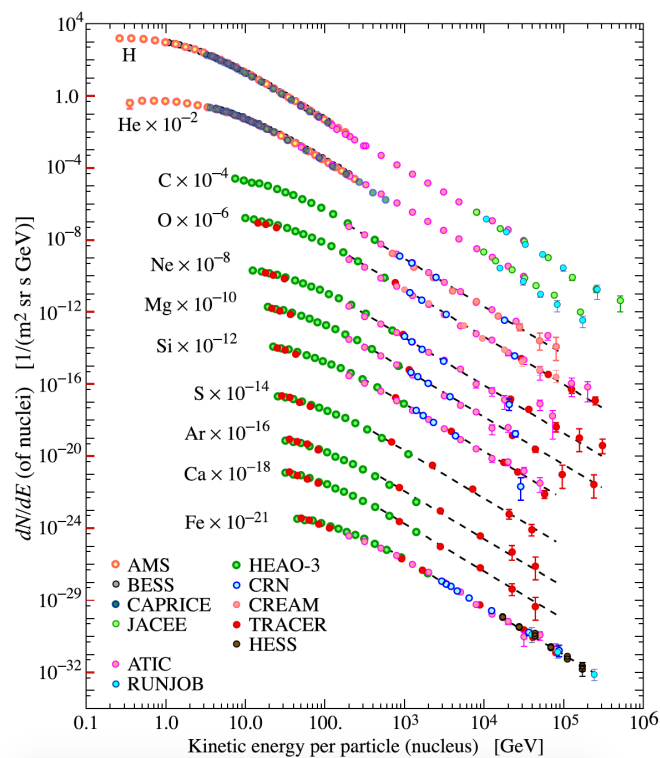


Figure 2.8: Cosmic Rays spectrum: flux of nuclei (particles per-energy-per-nucleus) vs kinetic energy per particle. From: [23]

of GCRs fluxes is observed when the solar activity increases. This occurs due to the deflection of cosmic rays when interacting with the magnetic fields embedded within the solar winds. From this, we conclude that for periods of more/less intense solar activity (solar maximum/minimum) we have a high/low attenuation of the GCRs. This can be a significant factor when planning long period missions.

Table 2.2: Main sources and characteristics of radiation near-Earth orbit. Adapt from: [22]

Radiation	Maximum Flux ( $\text{cm}^{-2}\text{s}^{-1}$ )	Radiation Effects	Shielding Effectiveness
GCRs	$\sim 10$	SEE	Low
SPEs	$\sim 10^5$	TID,DD,SEE	Moderate
Trapped electrons	$\sim 10^6$	TID,DD,ESD	High
Trapped protons	$\sim 10^5$	TID,DD,SEE	Moderate

#### • Solar Particle Events

Solar particles like electrons, protons, and heavier ions (from He to U) can be found everywhere in the interplanetary space and may present energies from 10 up to  $10^2$  MeV. These particles may be produced by two types of solar events namely Solar Flares (SFs) and Coronal Mass Ejections (CMEs). The former is rich in electrons and occur due to the release of the excess of energy accumulated in the coronal magnetic field in the form of a burst of energy (electromagnetic radiation, electrons, and protons) which may occur due to magnetic reconnection [24]. The latter is characterised by higher proton fluxes, and the released energy occurs when an unusual large amount of matter is expelled from Sun's surface. This type of radiation affects predominantly missions at high planetary orbits as well as missions outer of space since there is no natural magnetic shielding out there. Still, the high unpredictability of solar events is another important aspect that must have to be taken into account during the planning of a long-duration mission far from Earth.

#### • Trapped Charged Particles

Around the Earth, for altitudes between  $10^2$  to  $10^4$  kilometers, it is possible to distinguish two main regions where numerous electrons and protons are confined within the geomagnetic field lines, as we can see in the Figure 2.7. These regions are known as the Van Allan radiation belts. The electrons (outer belt) and protons (inner belt) that reside in these regions can have energies ranging from  $\sim 0.1$  to 10 MeV and  $\sim 0.1$  up to  $10^3$  MeV, respectively. Within the zone which separates the two belts (slot region), plasma populations with energies lower than 0.1 MeV may be found.

### 2.3.2 Space radiation effects

When a component is sent to space, there is a higher probability to be exposed to very high energetic radiations, which may lead to internal and external modifications. In order to have functional devices performing in space, is important to examine properly what is the radiation damage on device properties. Different kind of hazards may result from radiation-matter interactions which may depend on the source of radiation and its energy, dosage, and materials features like crystallographic structure and ordering,

composition and grains size. The main forms which radiation effects may be pronounced are: total ionizing dose, displacement damage, single event effects, and electrostatic discharges.

- **Total ionizing dose (TID)**

TID effects represent the damage associated with the accumulated dose of ionizing radiation by a material, and so, it can be seen as a long-term effect of radiation. A very good knowledge about TID effects is important in order to plan a long duration space mission.

TID is considered as being the main mechanism of cumulative radiation damage in charge-based technologies. Its effects have more impact on materials like oxide insulators (such as  $\text{SiO}_2$ , which has dielectric properties and is used in technologies like MOS), since they have very low concentration of free charges (due to the large gap between the valence and conduction bands) comparatively to conductors and semi-conductors. This makes insulators' electrical properties more susceptible to modifications when facing ionizing radiation. The physical process presented in Figure 2.9 describes the radiation response when ionizing energy is deposited within a dielectric material [25], and may be outlined by the following sequence:

1. Electron-hole pairs (ehps) are produced due to the ionization of electrons (by Photoelectric effect, Compton effect, or electron-positron production) from the valence band of a material (leaving, then, a hole) to the conduction band;
2. Some of the generated ehps recombine rapidly after their generation ( $\sim\text{ps}$ ), while others do not;
3. Electrons and holes that did not recombine, will be transported in direction of the oxide/semi-conductor interface (if the gate is positively biased). During this transport, from interactions between the holes and hydrogen contained in oxide defects, protons are released;
4. Some of the holes will be trapped in long-term trapping sites (defect precursor sites) near interface and oxide bulk, leading to the formation of positively trap charges. Also, from interaction between the release protons and the adjacent material, interface traps will be formed [26].

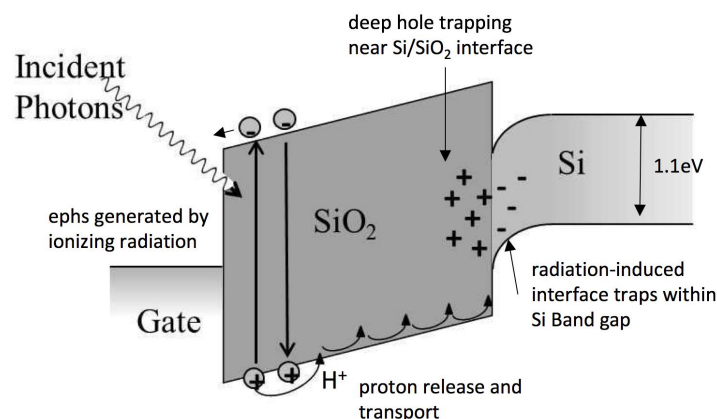


Figure 2.9: Scheme of ionizing radiation effects on energy band diagram of  $\text{SiO}_2$ . Adapt from: [5].

Some of the consequences from these radiation-induced effects (trap charges within the oxide bulk and interface) are shifts in the threshold voltages, increase of noise level, and degradation of devices, resulting from the buildup of localized potentials. Like within in CMOS technologies, also, in magnetoresistive technology, e.g. MTJs sensors, there is oxide material in their constitution like in the barrier, as well as around sensor structure as passivation material.

Still, from TID assessment is also possible to infer the amounts of ionizing doses that a device may withstand. This type of assessment is typically done according to standard procedures defined by space agencies, where Cobalt sources providing gamma radiation or electrons beams are used to exposed materials in order to inspect TID. These type of sources are considered to be standard sources since they represent well the conditions to which spacecraft and components are subjected at high planetary orbits, where the exposition to secondaries as gammas and to charged particles present in radiation belts are predominantly. In this work, a Cobalt source was used.

- **Displacement damage (DD)**

Displacement damage is a non-ionizing phenomenon which is associated with the displacement of an atom from the space lattice of a material. When passing throughout a material, high energetic particles (typically protons) may transfer their energy through their deceleration along the material causing excitation of the atoms, and due to elastic collisions with lattice atoms. The latter one is associated with DD. Depending on their energy, radiation particles may provoke the formation of unstable clusters and isolated defects due to the dislodging of atoms within the lattice leading to the creation of interstitials, leaving behind empty spaces named as vacancies. Depending on the energy gained by the displaced atom, secondary displacements may occur. Most of the time (90%), reconnection interstitial-vacancy occurs. If not, by migration, pairs of interstitials and vacancies may be formed leading to the formation of stable defects (Frenkel's pair) within the lattice. Under a low particles fluence ( $\Phi$ ) regime, the amount of displacements within a material may be quantified as,

$$c = \Phi A(NIEL), \quad (2.3)$$

where A is a parameter which accounts for the portion of non-recombined atoms shortly after irradiation. NIEL (non-ionizing energy loss) quantifies the rate of energy density (normalized) which was lost by incident particles due to displacements. J. R. Srour et al. (2003) [27] did a very good review about the radiation-induced displacement effects on silicon-based devices. Due to the high amounts of energy and the physical mechanism associated to displacement damage, typically high degradation of components occurs when compared with TID's effect.

- **Single event effects (SEE)**

SEE may be considered as an unexpected and instantaneous effect, since they are related with a quick absorption of a large amount of energy associated to an isolated high energetic event as, for example, the incidence of a high energetic cosmic ray on a component provoking rapid modifications on it.

- **Electrostatic discharge (ESD)**

ESD is related to the difference of potential between surfaces, since different surfaces may have different charge densities. In space, these potentials may be build-up normally due to the impinging of hot electrons carried by a plasma. If the voltage between two surfaces separated by a dielectric medium is higher than his breakdown voltage, then an electrostatic discharge can occur.

The type of radiation damage assessed in this project was the one associated to TID effects. This evaluation is important since MR sensors are expected to have a high life time on space. So, it makes sense to evaluate the long-term effect of radiation on the component. The common unit of TID is the Rad (S.I. unit Grey), where one 1 rad (0,01 Gy) is equivalent to 0,01 J of absorbed radiation dose by a 1 kg of the target material.

## **2.4 Radiation hardness assurance**

Typically, for a device to be sent into space, first it must pass through exhaustive qualification processes, which consists on the passage for different kind of tests like radiation, mechanical, thermal, among others. These processes can take some time until the verification of the desired maturity level of some component, i.e., once it has given the necessary proves that is highly probable that the component will not stop working, once in space, during the period of time of a mission. In order to have to distinguish better in which phase of readiness a component under qualification might it be, space community introduced the "Technology Readiness Level" (TRL) concept. TRL, basically, categorizes a device depending on what it was already proven to be capable of under specific conditions. The TRL classification is illustrated in the Figure 2.10. Since of the end of the 90's and beginning of the 20 century that Anisotropic and Giant magnetoresistive sensors have been used in space missions. These are inserted at level 9 of TRL diagram. The work done in this project would correspond to a lower TRL like level 3, since TMR and GMR sensors with general purposes were evaluated here.

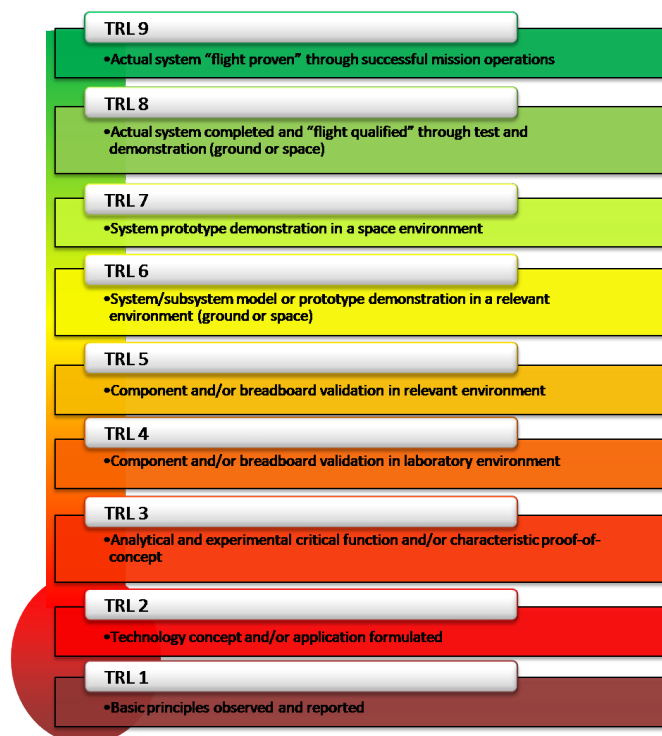


Figure 2.10: TRL diagram. From: NASA



# Chapter 3

## State-of-the-art

Now that the main background concepts were established, I will give some insight of some of the works already done, related with the effects of radiation on magnetoresistive technology and their radiore-sistance. First, we will see the response of magnetic materials when submitted to different types of radiation. Then we focus more on the radiation effects on magnetoresistance sensors and how these may influence the performance of a device.

### 3.1 Radiation damage in materials

Since the 50's and 60's that interest in the nature of radiation effects on magnetic materials started to emerge. Gordon and Sery (1964) [28] presented a summary of some of the first experimental results related to the investigation of the effect of the bombardment of magnetic materials with neutrons and high energetic charged particles. From most of the results, it was observed that soft magnets such as nickel-iron alloys suffer variations on their structure-sensitive properties like in hysteresis loops, coercive fields, remanence, and permeability associated to modifications within internal microstructures as magnetic domains. Many of these changes were verified to be reversed. Another interesting aspect was that some type of material's stresses and defects are more sensible to be detected by the inspection of magnetic properties of materials than the electrical ones (like resistivity, density changes, stored energy).

In 1973, Tench and Duck [29] observed that a MgO insulator was intrinsically modified when bombarded with 20 MeV protons. This modification (provoked by displacement damage) was considered to be a result of the creation of vacancies (of anions or cations, being these initially generated by ionizing radiation) in the lattice space of the material. These may change material's band gap as, for example, by creating localized states between the valence and conduction bands due to the charge trapping, so, changing its electrical properties [5].

## 3.2 Radiation effects on magnetoresistive sensors

In the beginning of 2000, first studies about radiation damage in SV structures started to be published. Guo et al. (2001) [30] did the irradiation of SVs, composed by IrMn/CoFe/Cu/CoFe/NiFe, with 30 keV Ga<sup>+2</sup> and observed a decrease of exchange bias and MR signal, as also the increment of resistance with the increase of ion doses. Exchange bias changes induced by irradiation may be consequence of the competition between pinning and interfacial mixing at the FM/non-magnetic interface verified as ion dose increase, while the increase of resistance may be associated to the generation of bulk defects as also to the atomic interfacial mixing. From gamma irradiations of SVs (Si / SiO<sub>2</sub> 3000/ Ni<sub>80</sub>Fe<sub>20</sub> 100 / Cu 61 / Ni<sub>80</sub>Fe<sub>20</sub> 100 / Fe<sub>50</sub>Mn<sub>50</sub> 200 / Ge 100, with the numbers representing the thickness of the layers in angstroms) to a dose up to 50 Mrad, Carroll (2010) [31] shown that the sensors kept their functionality, though, small changes (variations of 4 and 6 Oe were observed) in coercivity and a decrease trend of the MR signal (overall decreases of 0,15 to 0,44 % were noticed) were verified while exchange bias was observed to be rad hard.

Conraux et al. (2003) [32] presented results from the bombardment of AlOx-based MTJs with high energetic (10 MeV/A) heavy ions, where an irreversibly small decrease in TMR amplitude with the increase of ion fluence was observed. Minimization of global magnetisation and spin-polarized current were the attributed main causes to TMR's decrease, which have resulted as consequence of the modifications on the magnetic domains and creation of defects in the materials induced by irradiation. Also in this work, in order to inspect radiation effects on FM/Al<sub>2</sub>O<sub>3</sub>, spin mirrors were irradiated with 756 MeV Kr<sub>84</sub><sup>31+</sup> which translated in the decrease of GMR amplitude.

Han et al. (2008) [33] observed another interesting fact where a higher enhancement of MR signal plus the simultaneous increase of the exchange bias of spin-valves, by using H-ions (550 eV) irradiation instead of the typical annealing process, was achieved. It was stated that the origin of this enhancement when compared with the one obtained for spin-valves in which annealing treatment is carried out, may be due to the lower radiation-induced intermixing between magnetic layers.

A very good review article on radiation effect of MR sensors is presented by Lu et al. (2014) [34], where AMR sensors displayed in a Wheatstone configuration, appeared to be resistant to irradiation with gamma rays for values of TID until 200 krad. In other study [9] from the analysis of TID effects of 200 krad in AMR sensors in Wheatstone bridge configuration, it was shown that the sensors only suffered small performance degradation (with errors for the sensing field lower than 10 nT).

In order to evaluate TID effects on MR sensors, biased single MgO-based MTJs were exposed to doses of gamma radiation up to 10 Mrad [5]. No signs of device's performance modifications, neither in terms of its magnetic (coercivity and TMR signal) and electric properties, were observed. Still on the evaluation of TID effects, Arias et al. (2015) [19] have irradiated MgO-based MTJs current sensors configured in a Full Wheatstone bridge with X-rays up to a dose of 43 krad. They noticed that neither the MR signal nor bridge resistance were affected. Nevertheless, during irradiation, sensitivity and hysteresis suffered small decreases. Sensitivity was recovered, while hysteresis has reached higher values in a

post-irradiation period.

During the search of radiation effects in literature, it was noticed that there are fewer works about the effects of gamma radiation and so TID effects, when compared with the works where irradiation with charged particles are used.



## Chapter 4

# Sensors designs, fabrication process and characterisation methods

In this chapter, I start by presenting the design used to fabricate a sensor, based on TMR effect. The chosen design was strategically thought in order to fit the requirements settled by a parallel project from a collaboration between INESC-MN and Valencia University's researchers where the fabrication of a device capable to measure an electrical current was the goal. Nevertheless, for my dissertation the main focus was not to explore and apply the sensors in a device able to measure currents, but to assess its behaviour after subjected to high dose levels of ionizing radiation in order to understand if the sensor would withstand in harsh environments like space. Along the chapter, I also described what were the fabrication processes (which can be seen below), the implementation of the sensors, and also a brief explanation of the operating principles behind every machine used. A more detailed version of all of the fabrication steps may be found in the run-sheet in the Appendix A. In the end, it is mentioned how and what were the techniques used to characterise the sensors.

Adding to the fabricated sensors (AlOx-based MTJ), two more types of MR sensors (SV and MgO-based MTJ) were provided in order to assess their radiation tolerance. These two type of sensors were not fabricated by my self, but only tested for radiation.

### • Fabrication steps

1. Deposition of MTJ stack
  - (a) 1<sup>st</sup> Lithography
  - (b) MTJ stack deposition
  - (c) Lift-off
2. Deposition of MTJ stack with e.a. reversed relative to the 1<sup>st</sup> one
  - (a) 2<sup>nd</sup> Lithography
  - (b) MTJ stack deposition
  - (c) Lift-off
3. Bottom electrode definition
  - (a) 3<sup>rd</sup> Lithography
  - (b) Etching

- (c) Resist-strip
- 4. Definition MTJ pillar
  - (a) 4<sup>th</sup> Lithography
  - (b) Etching
  - (c) Oxide deposition
  - (d) Lift-off
- 5. Ru temperature sensor
  - (a) 5<sup>th</sup> Lithography
  - (b) Deposition of Ru
- (c) Lift-off
- 6. Top electrode deposition
  - (a) 6<sup>th</sup> Lithography
  - (b) Metalization
  - (c) Lift-off
- 7. Vias
  - (a) 7<sup>th</sup> Lithography
  - (b) Oxide deposition
  - (c) Lift-off

### 4.1 Current sensors based on TMR effect - proposed design

As it was already mentioned in section 2.2, in order to have a current device with the desired large and stable output over a wide range of temperatures, the chosen design to fabricate the device was a full Wheatstone bridge configuration. The autocad mask used for the fabrication is presented in Figure 4.1.

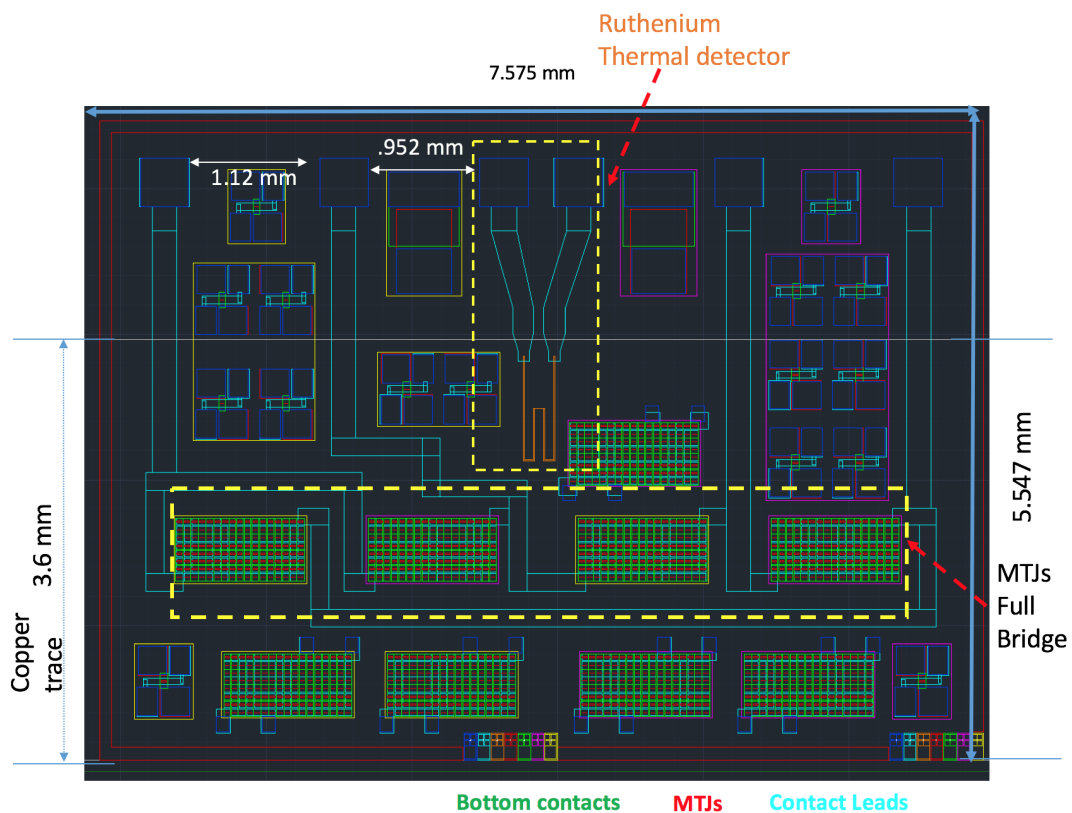


Figure 4.1: Current sensor autocad design. The full Wheatstone bridge is displayed in line. Each of the four sets of resistors are constituted by 136 MTJs connected in series. Software Autocad 2015

The bridge was constructed in line in order to measure an electric current which was supposed to flow through a copper line on a printed circuit board. Each resistor of the Wheatstone bridge is composed by 136 MTJs connected in series. This provides higher electrical robustness to the bridge. Each junction has an area of  $2 \times 40 \mu\text{m}^2$ . The mask also presents test structures like single and series of MTJs, and also a Ru temperature sensor, which was a requirement of the project in order to monitor the effect of temperature drift on the device performance. This last feature was not used during the project.

## 4.2 SVs and MgO-based MTJ sensors - features and designs

Two more types of MR sensors were used in this project, SVs and MgO-based MTJs. Their autocad designs are presented in Figures 4.2 and 4.3.

The SVs sensors (36SV2845) were fabricated with the purpose of SV optimizations. The sensing area of these sensors is  $100 \times 2,5 \mu\text{m}^2$ , and they are constituting by the following stack ("elements" "thickness in angstroms Å"): NiFeCr 50 / NiFe 28 / CoFe 22 / Cu 22 / CoFe30 / Ru 8 / CoFe 26 / NiFe 7 / MnNi 300 / NiFeCr 90.

In Figure 4.3, we can see that the MTJ sensor (TJ937) was composed by 26 individual MTJs connected in series. Each junction has an area of  $100 \times 100 \mu\text{m}^2$ , being each MTJ composed by ("elements" "thickness in angstroms Å"): Ta 50 / Ru 150 / Ta 50 / Ru 150 / Ta 50 / Ru 50 / IrMn 200 / CoFe<sub>30</sub> 20 / Ru 8.5 / CoFe<sub>40</sub>B<sub>20</sub> 26 / MgO 10 / CoFe<sub>40</sub>B<sub>20</sub> 20 / Ta 2.1 / NiFe 40 / Ru 2 / IrMn 60 / Ru 20 / Ta 50 / Ru 100. These sensors were produced in order to have a resistance area product ( $R \times A$ ) of  $40 \text{ k}\Omega \mu\text{m}^2$ , and the final application was to detect buried defects within materials [35].

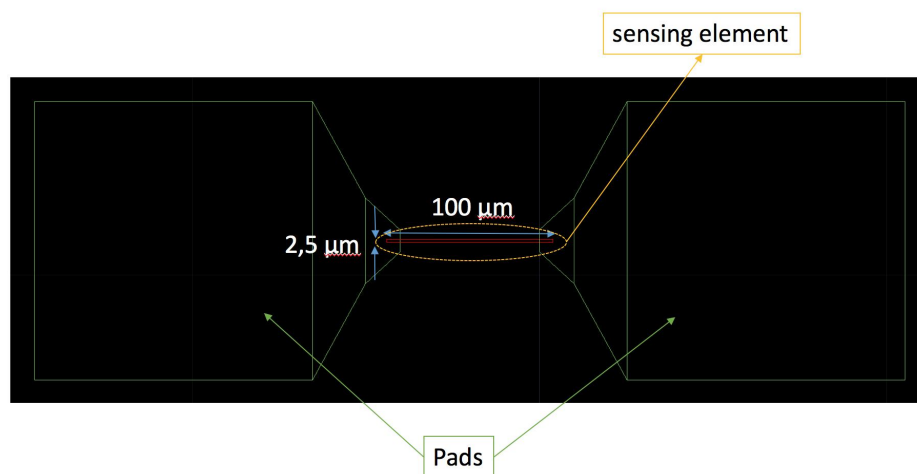


Figure 4.2: SV autocad design. Software: Autocad 2015

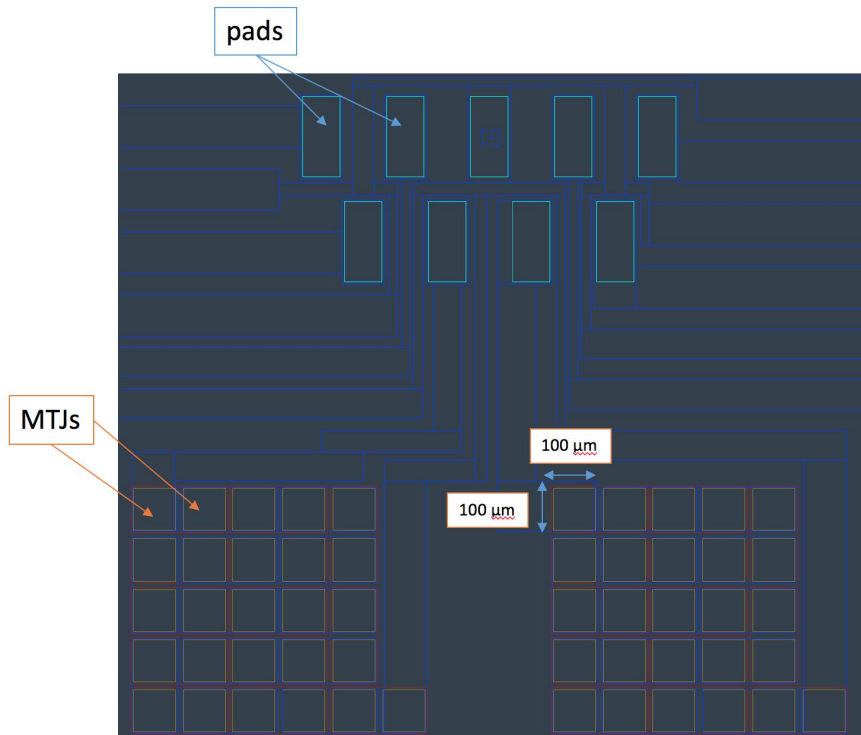


Figure 4.3: MgO-based MTJ autocad design. Software Autocad 2015

## 4.3 Current sensors micro and nanofabrication process, and sensors implementation

### 4.3.1 Deposition of MTJ stack

- 1<sup>st</sup> Lithography

The first fabrication step was to pattern the sample by creating structures where we wished to deposit the first stack of MTJ. The patterning was performed by a technique called photolithography, done with a Heidelberg DWL 2.0 system shown in Figure 4.4 (bottom). This system uses a laser beam, with 405 nm wavelength and a spotsize of  $0.8 \mu m^2$ , which is focused onto a properly aligned sample, through an optical system, in order to draw the desired features. Depending on the regions to be exposed in a virtual mask read by the machine, the laser is switched on and off by a control system. The sample is moved by a moving stage in steps of  $200 \mu m$ . Before proceeding to the laser exposure, a coating layer of a polymer, which the laser will interact with, called photoresist (PR) must be applied to the sample. This coating process is done in a Silicon Valley Group (SVG) track system (Figure 4.4 (top)) and consists in two main steps:  $1.5 \mu m$  PR uniform deposition, and PR hardening by heating. There are two types of photoresist. One positive which basically will get weaker when the laser interacts with it, and negative one where the opposite occurs. After the exposure is done, a development process is carried out in order to have only the desired structures transferred into the sample by removing the undesired PR. Development of the sample consists on the following steps: the sample is initially heated in order to remove standing waves

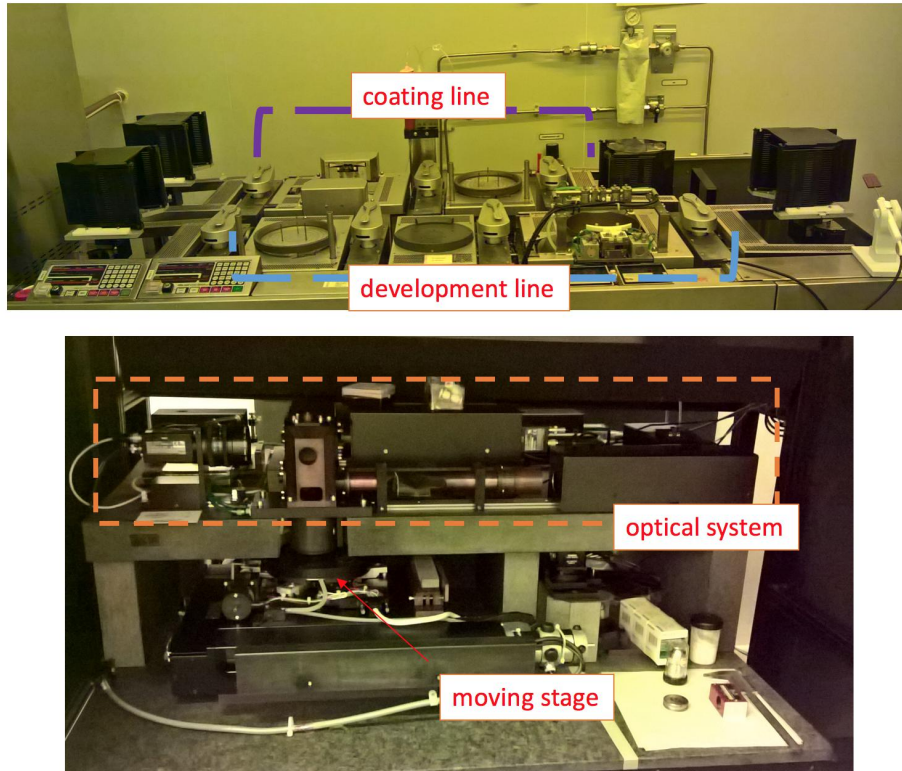


Figure 4.4: (top) SVG track and (bottom) Direct write laser.

inside the PR layer (to have a better shape of the PR), then the sample is cooled down and, to finish, it is subjected to the developer TMA238WA itself, a chemical reagent. Another important aspect that should be mentioned is, before the application of the PR coating, the sample should always be subjected to a specific atmosphere and temperature (vapor-prime) which ensures a better adhesion of the PR to the sample. The coating and development recipes, and also some informations about the exposures can be seen in the run-sheet found in the Appendix A.

- **1<sup>st</sup> deposition of MTJ stack**

The second step was the deposition of a top-pinned MTJ stack within the regions defined in the 1<sup>st</sup> lithography. The deposited stack was the following one: Ta 50 / [Ru 150/ Ta50]x3 / NiFe 30 / CoFeB 30 / Al 8 (Ox 30") / CoFeB 30 / Ru 6 / NiFe 30 / MnIr 180 / Ru 150 / Ta 50 , with the thickness in angstroms. The choice of this stack had to do with the requirement of having a bridge resistance of 2 k $\Omega$ , and also due to mask features like the fact of having 136 junctions (in one resistor) and their geometry (2x40  $\mu\text{m}^2$ ). So, a stack with an 1,2 k $\Omega \cdot \mu\text{m}^2$  was used as required. As seen in section 2.1.3 (page 11), different functions are associated to different layers and combination of layers which compose the stack displayed in Figure 4.5 (left).

The deposition was done in an ion beam system - Nordiko 3000 - which can also be used for ion milling processes. A scheme of the machine's interior is shown in Figure 4.5. The machine has two chambers. One called loadlock, where the sample is firstly placed. The sample is ready to be transferred to the main the chamber once a the proper vacuum level (low vacuum  $\sim 10^{-5}$  Torr) is reached inside of the

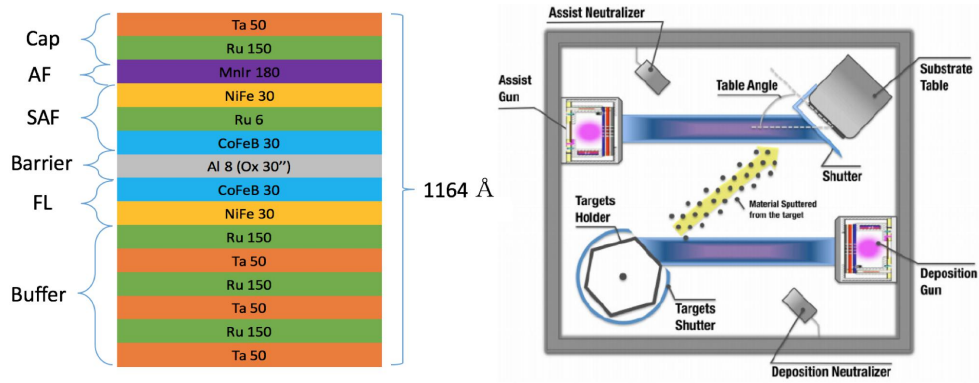


Figure 4.5: (left) MTJ stack which was deposited. (right) Scheme of the ion beam system.

loadlock. At the main chamber an ultra high vacuum  $\sim 10^{-7}$  Torr exists and it is where the deposition occurs. The existence of a loadlock chamber is fundamental to avoid the pressurization of the main chamber. This allows the risk of contamination in the depositing films and the targets to lower. Typically, the machine has 6 targets available, composed by different materials for deposition. The machine has two main guns. Inside of each gun, a plasma is produced. By the application of a potential difference between the grids of the gun, it will be possible to create a separation of charges. Then, the positive ions will move in the direction of the negative grid and will create a focused beam after passing through an optical system. This beam will sputter a target at a specific angle in order to the expelled material to be directed to the substrate and ending up to be deposited there. Close to the substrate, a constant magnetic field is applied. This magnetic field will allow the formation of the pinned layer, by inducing the formation of a material with a well defined e.a..

- **Lift-off MTJ1**

After deposition, the unwanted material was removed by placing the sample inside a beaker with an organic solvent called FujiFilm Microstrip 3001 activated at 65 °C of temperature and with ultrasounds, which was done inside of the wetbench. The micro-strip will react with the PR layer, ending up by removing it as well as all of the material which was deposited on top of it (that is why it has the name 'lift-off'). After this process was done, the sample presented the MTJ stack only within the exposed regions during lithography accordingly to the non-inverted mask. The result was the deposition of two resistors of the full Wheatstone bridged plus some test structures. Every lift-off process done during the fabrication of the sensors was always under the same conditions as the ones mentioned here. Also, after every lift-off and resist strip process, the sample was always cleaned with acetone, then isopropanol (IPA), and in the end with deionized water (DI water). After it, the sample was dry with compressed air.

### 4.3.2 Deposition of MTJ stack with e.a. reversed relative to the 1<sup>st</sup> one

- **2<sup>nd</sup> lithography**

To obtain the complete full Wheatstone bridge configuration a new lithography was done, again, with

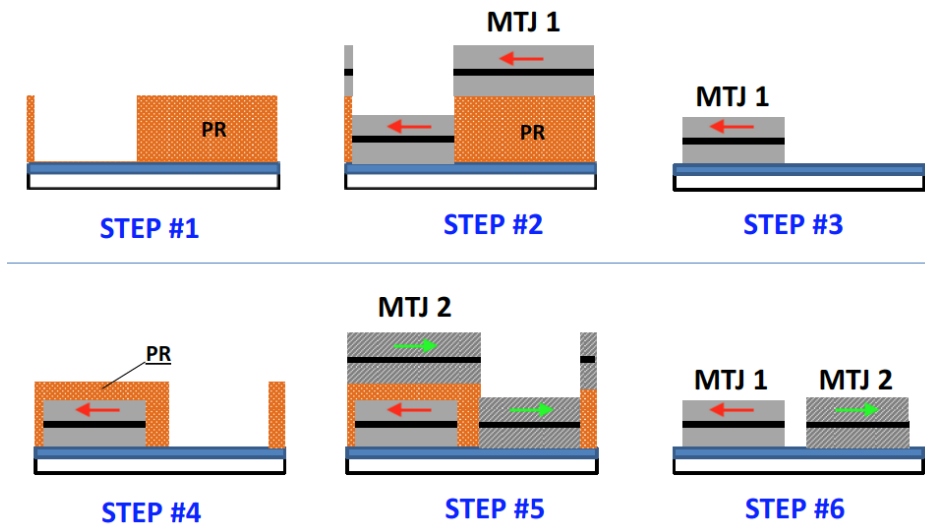


Figure 4.6: Stack deposition in a two step process in order to get the two reversed e.a.'s, identified by the red and green arrows. Adapt from: [6].

another non-inverted mask which had the pattern for the deposition of the remaining Wheatstone bridge resistors. So, here, the coating layer avoids the deposition of the second MTJ stack, done in the next step, on top of the already existent one.

- **2<sup>nd</sup> deposition of MTJ stack**

In order to have the Full Wheatstone bridge, a second deposition step was done. The two deposition process is presented in Figure 4.6. For the second deposition, the same MTJ stack was used as in the first deposition, the only difference was the direction of the e.a. which was rotated about 180 ° relative to first one defined during the 1<sup>st</sup> deposition.

- **Lift-off MTJ2**

After the deposition, another lift-off process was done. This allowed the possibility to construct the full Wheatstone bridge by working the initial four unprocessed stacks structures disposed in line, as we can see in the mask in Figure 4.1, with alternate e.a. directions between each blocks.

### 4.3.3 Bottom electrodes definition

- **3<sup>rd</sup> lithography**

In this third lithography an inverted mask was used. This mask defined the shape of the bottom electrodes of the MTJs sensors. Two configurations of MTJs were defined, series of MTJs for the bridge and single MTJs working as test structures as it is possible to see in Figure 4.7.

- **Etching**

After the bottom electrode definition, a process to remove material from the unprotected regions was done. This process was also done in Nordiko 3000, but now with the ion milling system. Instead of the

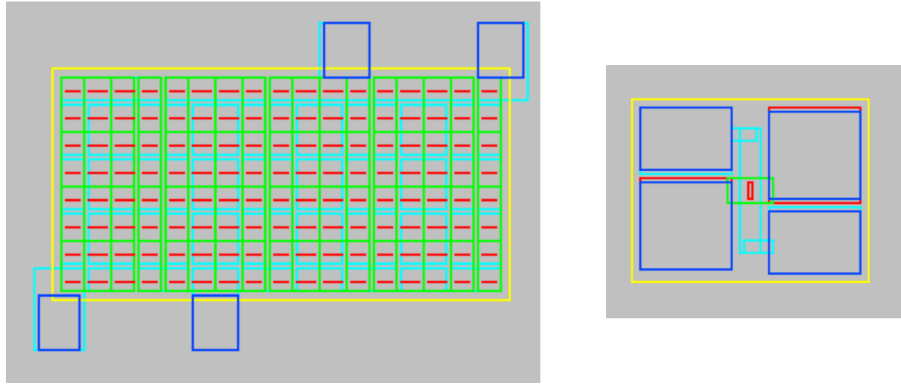


Figure 4.7: (left) Resistor with 136 MTJs connected in series. (right) Single MTJ. Color scheme: (yellow) region where was deposited MTJ stacks, (green) bottom electrodes, (red) MTJ pillar, (cyan) top electrodes, and (blue) vias.

deposition gun, an assist gun which points directly to the substrate was used. Similarly to the deposition gun, a plasma is generated and an ion beam will be formed from the extracted positive ions ( $Ar^+$ ). The incidence of the beam in the substrate may occur with an angle between  $10^\circ$  and  $70^\circ$ , between the gun and the substrate table, depending if a vertical profile is desired. For the bottom electrodes, the MTJ stack was etched at an angle of  $70^\circ$  and with an etch rate of  $\sim 1 \text{ \AA/s}$ . Other informations about etching conditions may be found in the run-sheet.

- **Resist strip**

After the remotion of the unwanted MTJ stack, the PR protecting layer is striped off from the top of the defined structures. This process is very similar to the lift-off where the sample is also immersed in the micro strip solution at  $65^\circ$  with ultrasounds. The difference is that the resist strip only removes the PR because there is no material on top of it.

#### 4.3.4 MTJ pillar definition

- **4<sup>th</sup> lithography**

The next step was the definition of the MTJs pillars. For this, again, an inverted mask was used in order to define the pillars shape. After the lithography, the sample was carefully inspected to see if the PR shape was well defined and if their dimensions were the same as the ones we wanted to transfer for the pillars. The pillars were designed with an in plane area of  $2 \times 40 \mu m^2$ .

- **Etching**

Using Nordiko 3000 to remove material from the sample, it was possible to transfer the desired features to the top of some portion of the bottom electrodes. For this etching, two profiles were obtained, as we can observe in the scheme in Figure 4.8 (right), since two different angles between the assist gun and the substrate were used. Initially, the sample was etched approximately with a vertical profile, i.e., with a pan angle of  $70^\circ$ . This first etch was done until the end of the oxide layer. The second etch was done

with an angle of  $40^\circ$  in order to remove possible detriments re-deposited at the barrier. From this etch, also resulted the removal of material from the FL until the first layer of Ta associated to the buffer.

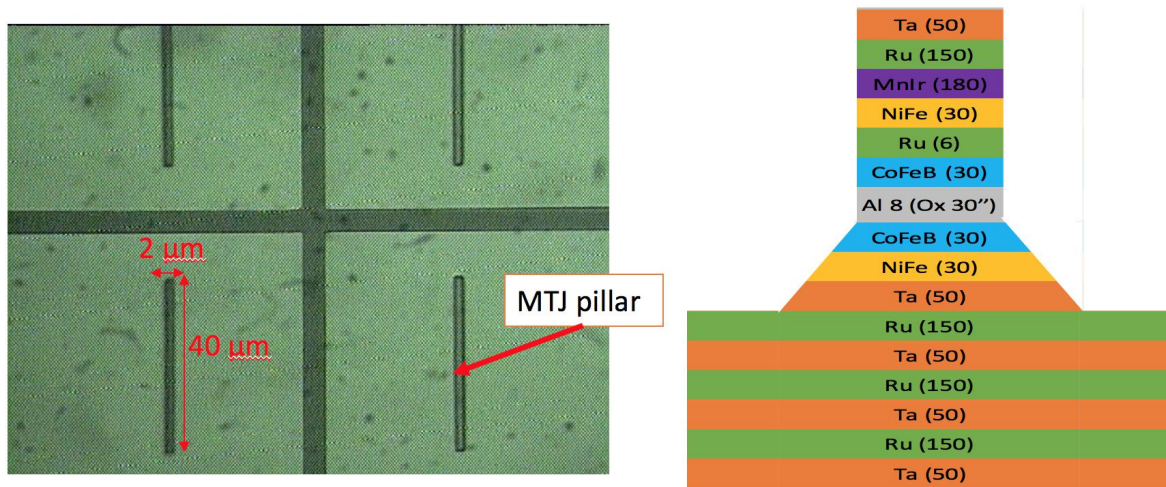


Figure 4.8: (left) Microscopic image of the pattern of the MTJ pillars. (right) Scheme of the stack structure that is expected to be transferred after the etching of the pillars.

- **Oxide ( $\text{Al}_2\text{O}_3$ ) deposition**

After having the pillars well defined, still with the PR on top of them, aluminum oxide commonly called alumina ( $\text{Al}_2\text{O}_3$ ) was deposited up to a thickness superior to the one associated to the pillars. This deposition was done in a RF sputtering system (UHV2). This system only has one chamber, so every time we wish to deposit, it is needed to vent and depressurize the chamber. For the same reason and for this system, we need to wait up to 10-12 hours in order to obtain a good vacuum level ( $\sim 10^{-7}$  Torr) before starting the deposition. An Ar flow is injected onto the chamber. Then, a power of 200 W is applied, and a plasma discharge is initiated between the target (cathode) and the plate (anode). Ar gas will be ionized giving origin to the  $\text{Ar}^+$ . To increase the ionizing degree of the working gas, and so, to obtain a higher sputtering rate of the target, a magnetic field is applied by a magnetron located close to the target. The material sputtered from the target will end up by being deposited on top of the sample.

The thickness of the deposited oxide ( $1214\ \text{\AA}$ ) was bigger than the MTJ's thickness ( $1164\ \text{\AA}$ ). The reason for this was to avoid any electrical contact between any of the layers of the MTJ stack, except the top one (Ta), with the top electrode which was deposited in the next step, and also to protect the sensor.

- **Lift-off**

After the oxide deposition, in order to open the pillars, i.e., to clean the PR on top of them, lift-off was done. Due to the reduced pillars dimensions, this process took more time ( $\sim 8$  hours) than the other lift-off processes, in order to get all of the pillars redeemed of the PR.

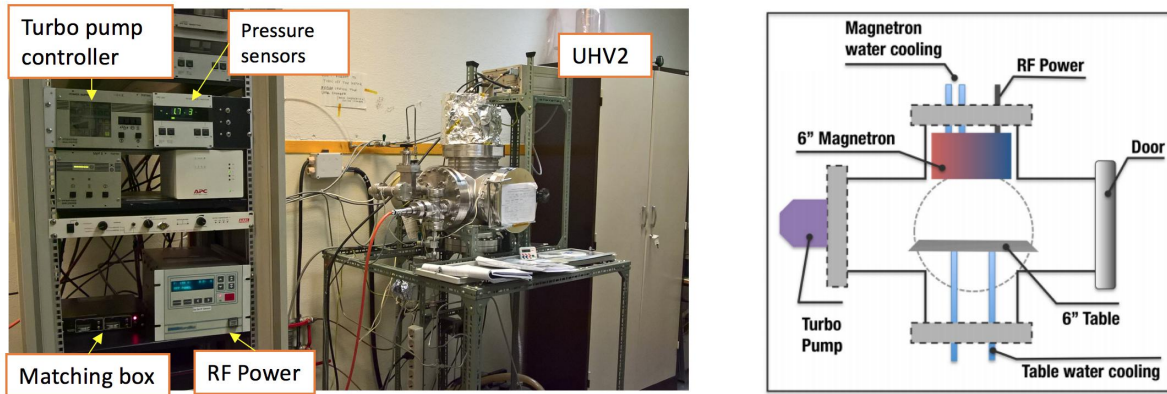


Figure 4.9: (left) RF magnetron sputtering apparatus (UHV2 system). (right) RF magnetron sputtering scheme. From: [7]

### 4.3.5 Ru temperature sensor

- **5<sup>th</sup> lithography**

The purpose of this lithography was to pattern the structure of a temperature sensor observed at Figure 4.1. A non-inverted mask was used. Like I said in the beginning of this chapter, these feature was not used in these project.

- **Ru deposition**

The materials used for the temperature sensor were Ta 50 Å / Ru 400 Å. These were deposited in Nordiko 2000. The deposition method employed by this system is different to the one employed in the Nordiko 3000, where here, a sputtering deposition occurs.

- **Lift-off**

Again, to keep the Ru material only in the designated region, the unwanted material was removed by lift-off.

### 4.3.6 Top electrodes definition

- **6<sup>th</sup> lithography**

In this lithography, using a non inverted mask, were defined the top electrodes, the contact lines and the pads. Before exposure and after the PR coating, the sample was pre-developed during 20 seconds. Also more energy was used in the laser. These two variations were done in order to remove more easily the next deposited layer which was thicker than any of the other deposited layers.

- **Metalization**

After lithography, a layer of 1.2  $\mu\text{m}$  of an aluminum alloy (AlSiCu) was deposited at Nordiko 7000 (DC magnetron sputtering system). The sample was firstly placed inside of a loadlock chamber and stayed

there until a good vacuum was reached. Then, it was moved by a robot arm to inside of a dealer chamber. There are 4 modules as we observe in Figure 4.10. Each module has the following functions: 1) Flash annealing (not used); 2) Sputter etch; 3) TiW deposition; 4) AlSiCu deposition. The sample was delivered first to module 2, where an etch of 1 minute was executed in order to clean possible oxidative residues on top of the sample, in particular over the Tantalum film at the pillar. Next, the arm moves the sample to module 4. It is in this module where the AlSiCu layer is deposited in 4 steps. The process is finished with the deposition of  $150 \text{ \AA}$  of  $\text{TiWN}_2$ , in module 3, to prevent oxidation.

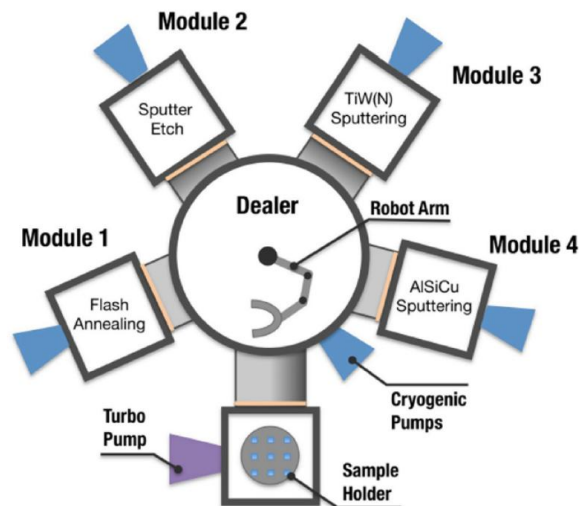


Figure 4.10: Nordiko 7000 modules scheme. From: [7]

- **Lift-off**

In order to have only the top electrodes, the pads and the contact lines in the created cavities, a lift-off process was performed.

### 4.3.7 Vias

- **7<sup>th</sup> lithography**

The last lithography had the purpose to protect the pads of the bridge and test structures from the final passivation. Otherwise, it would not be possible to access to any element on the chip. So, an inverted mask was used to pattern the vias.

- **Oxide ( $\text{Al}_2\text{O}_3$ ) deposition**

For the final passivation about  $1500 \text{ \AA}$  of alumina was deposited in order to protect the device. The passivation was done again in the UVH2.

- **Lift-off**

In order to unveil the pads of the sensors, lift-off was executed. After this, the metal pads remained

available again in order to characterise the sensors. This was the last process of fabrication of the device. The next steps were the separation of the dies and the implementation on chip-carriers.

### 4.3.8 Dicing

During all of the fabrication, a sample with 18 dies was worked. To separate each die, it was used a dicing saw machine, Disco DAD 321. Having into account the parameters for the size of the dies, an automatic cut was performed. Other parameters like the tape height, blade width, cut speed, sample size are important. Before cutting, the sample was glued to a tape in order not to lift away during the procedure.

### 4.3.9 Wire bonding

After the separation of the dies, the sensors were implemented on chip-carriers. The wire bonding of the sensors to the chip was done with the system presented in Figure 4.11 (top left). The wire bonding is done with aluminum wire, with  $45 \mu m$  of diameter, which is attached to a needle. Two weld points are done in order to make a connection. The welding is done by the combination of the force applied by the needle on the pads of the sensors/chip plus ultrasounds which melt the wire. Since these wires are fragile, the sensors were covered with silicone in order to protect them. Then, acrylic squares with

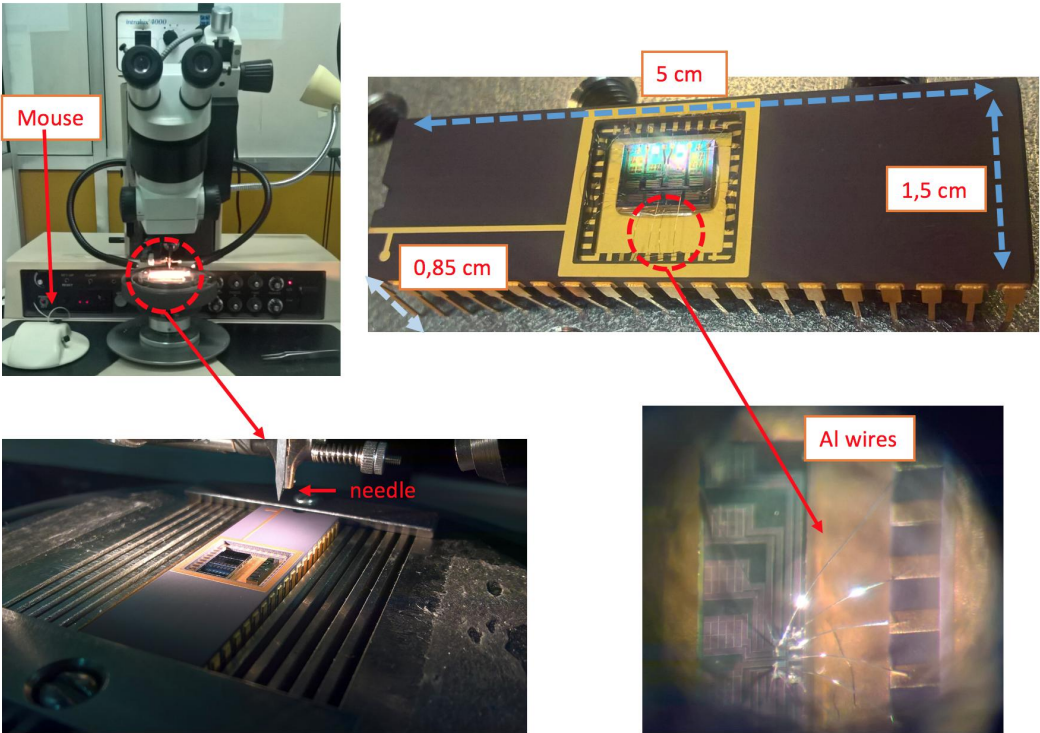


Figure 4.11: (top left) Wire bonding machine, and (bottom right) microscope view of the connections made by the needle when moved with a mouse to the desired regions. (top right) Chip-carrier with the implemented sensor.

1 mm thickness were glued in the top part of the chip-carriers in order to provide more protection to the sensors. In Figure 4.11 (top right) we can see a sensor implemented on a chip-carrier, where is also possible to see the thinny contact wires.

## **4.4 Characterisation methods**

### **4.4.1 Magnetotransport characterisation**

After the sensors were finished, I proceeded to their characterisation, i.e., the assessment of their magneto-transport properties through the measurement of the transfer curves of the sensors. Parameters like MR, resistance and potential difference when applying a magnetic field were obtained. These measurements were done by using a manual setup - setup 140 Oe - observed in Figure 4.12 (top). The varying magnetic field is created by the change of amplitude and direction ( $\pm 4$  A) of a current, generated by a bipolar DC current source system (Kepco), flowing through two Helmholtz coils. For the characterisations of the sensors, we first should bias them with a current (current source) or a voltage (sourceter), depending on the configuration of the sensors. When the application of the varying field is turned on, for each point of the field, a potential difference is measured with a multimeter. All the three instruments are connected with a computer, through a GPIB connection in order to display the obtained data as represented in the schematic in Figure 4.12 (middle).

Before the implementation of the sensors on the chip-carriers, they were biased and measured with a two or four probes, composed by tungsten needles in their extremities, moved by micropositioners. After implementation, sensors characterisations were carried out in a proper chip-carrier connector linked to a pin board selector.

### **4.4.2 Profilometer**

Inspections of the thickness of structures within the sample are important, for example, in order to know how much oxide is needed (for the first passivation) and to find out how much was deposited by inspecting a test sample. These inspections may be done by Dektak 3030ST profilometer. This system works by sweeping a diamond tip in a straight line on top of a sample. In the case of existence of different thickness profiles, as the tip is dragged along the sample, it will be modulated by vertical displacements, being these associated to higher or lower exerted forces. This exerted force will be felt by a piezoelectric sensor, and so the displacements of the tip will end up by being converted into an electrical signal.

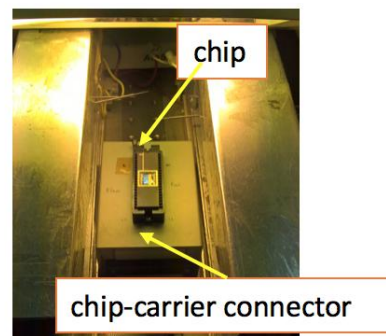
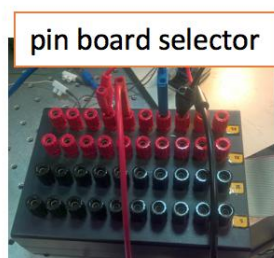
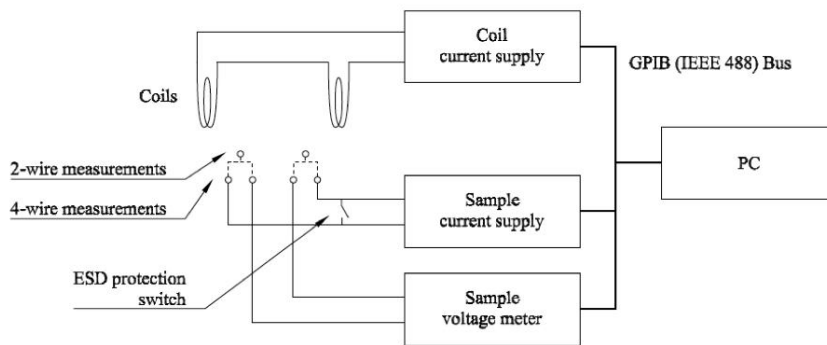
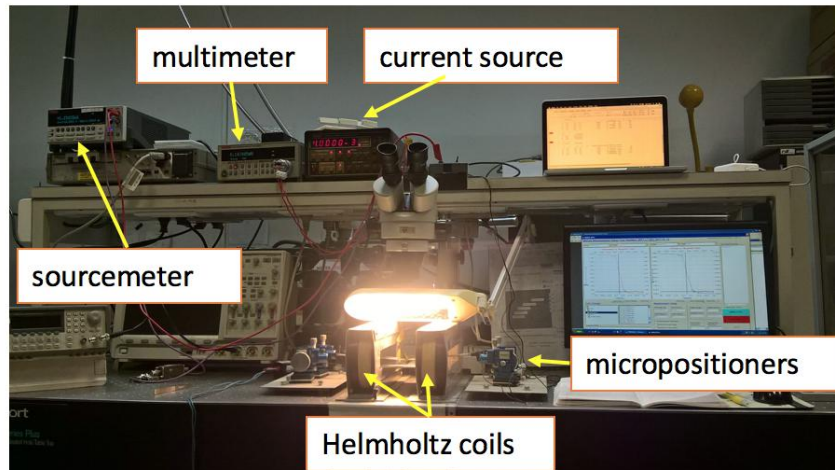


Figure 4.12: (top) Setup 140 Oe apparatus used for sensors characterisations. (middle) Setup electrical scheme. (bottom right) Chip-carrier connector and (bottom left) pin board selector.

## Chapter 5

# Irradiation and measurement of magnetoresistive parameters

This chapter describes the irradiation and characterisation of the MR sensors. The irradiation procedure is explained and the main results of the irradiation experiment of the MR sensors are provided and discussed. For more information about the irradiation protocol for the set of sensors which were irradiated see Appendix B.

### 5.1 Irradiation experiment

As it was already mentioned, the goal of this experiment consisted on the irradiation and the evaluation of the radioresistance of MR sensors. The irradiation was done with gamma radiation as a result from the decay of a Cobalt-60 source which has a half time of  $\sim 5$  years. The decay scheme of the Cobalt-60 nucleus is presented in Figure 5.1. Gamma radiation is known by being one of the most penetrating and energetic electromagnetic radiation. Irradiation tests using these sources for inspections of the long

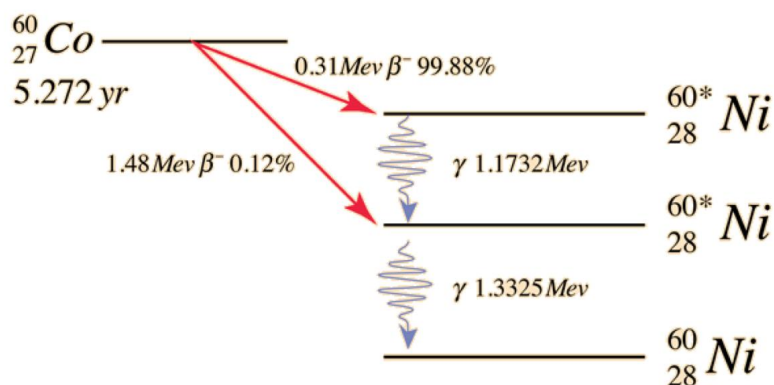


Figure 5.1: Co-60 decay scheme. Source: Hyperphysics

term effects of ionizing doses and qualification of components, are very frequent since they represent a worst case scenario like the case if the components were supposed to be launched on a spacecraft into space.

The goal of the irradiation procedure was to evaluate the radiation hardness of the tested MR sensors. The irradiation was performed with a  $^{60}\text{Co}$  gamma source at the Technological Unit of Radiosterilization at Campus Tecnológico e Nuclear - Instituto Superior Técnico (CTN-IST).  $^{60}\text{Co}$  gamma sources are used as standard sources for Total Ionizing Dose radiation testing for assessment of the long term effects of ionizing doses and qualification of components, representing a worst case scenario for the TID effects in components to be flown in space missions.

The decay scheme of the Cobalt-60 nucleus is presented in Figure 5.1, where it can be seen that it gives rise to two gammas with intensities of 1,17 MeV and 1,33 MeV. The  $^{60}\text{Co}$  gammas will interact with the materials of the EEE components, mostly by Compton Scattering with quasi-free electrons, which will lose energy inside the materials. The ratio between the energy lost by excitation and ionization of the media and the mass of the volume in which the energy was deposited corresponds to the absorbed dose.

Three steps of irradiation were done until an accumulated dose of  $\sim 5$  Mrad (50 kGy) was reached. Each irradiation step had the duration of  $\sim 1$  hour. In order to reach the desired total dose, the sensors were placed within a slot in a specific distance from the source. For that position the associated dose rate was 1.688 Mrad/h (16.88 kGy/h). This information was read a few days before the experiment. The total dose which the sensors were submitted, was monitored with a dosimeter (film badge dosimeter), which was placed close to the samples during the whole irradiation process. The total dose is obtained through the optical absorption of the dosimeter, which gets darker depending on the amount of radiation which it is subjected to.

The sensors were characterized after each irradiation step, in order to inspect the dependence of their studied parameters with total dose. The characterisation was performed at the INESC-MN facility. So, once each exposure was finished, there was a  $\sim 2$  hours and 30 minutes period in which the sensors were taken to INESC-MN, characterized, and taken back to CTN, before the next irradiation step. This strategy was followed in order to minimize the thermal annealing effect on the sensors which, for higher waiting times (between irradiation and measurements), might dissipate radiation-induced effects (if they exist) on the sensors.

So, the irradiation experiment consisted in three phases:

- before irradiation phase where the sensors were initially characterised;
- irradiation phase, which lasted one day, in which the sensors were irradiated in three steps and characterised (remotely) after each step;
- a third phase which corresponded to the inspection of the sensors in the following days (after 1 day, after 2 days, and after 1 month).

Only the characterisations associated to the irradiation phase were done in the same day.

## 5.2 Results and discussion

During irradiation, the sensors were always unbiased. Sensors characterisation before irradiation was performed right after the fabrication process, and after the sensors' implementation on the chip-carriers. The characterisation was essential to compare the initial state of one sensor to its response during and after irradiation. Also, the comparison between the irradiated sensors with the non-irradiated ones (reference samples) was crucial in order to distinguish what kind of variations may be or may not be associated to radiation effects. The data for the un-irradiated samples was obtained at the same period as the irradiated ones.

- **Measurement conditions**

For each type of sensor, different initial conditions were applied for the measurements.

- MgO-based MTJs - During characterisation, these sensors were biased with a current of 1,5 mA. For this current, biased voltages of around 157 mV were measured, which for the used geometry (presented in section 4.2 page 27) was equivalent of having  $\sim 4 \Omega$  per junction (and a voltage drop of  $\sim 6$  mV). This was consistent with the R.A product of  $40 \text{ k}\Omega \cdot \mu\text{m}^2$  associated to the stack.
- AlOx-based MTJs - full Wheatstone Bridges (WB) were tested. For these, a bias voltage of 1,5 V was applied in order to have a voltage drop of around  $\sim 5$  mV per junction. The equivalent bridge resistance was about  $1,2 \text{ k}\Omega$ . The R.A parameter associated with the implemented stack was about  $690 \Omega \cdot \mu\text{m}^2$ , half of what was expected ( $1,2 \text{ k}\Omega \cdot \mu\text{m}^2$ ), measured from the test structures.
- SV - The last type of MR sensors evaluated were the SVs. These were biased with 1 mA during characterisation.

About the software parameters, the data was obtained for a range of magnetic field between -141 to 141 Oe. Inside this interval, different field steps (in Oe) were used: 20, 4,2,1 for different field intervals. Field uncertainties are half of the step. The dependent parameter was measured 5 times for each value of the field. These points were taken after 0,5 s of the stabilization of the field.

The assessment of the parameters which characterise the performance of MR sensors like MR signal, saturate states, sensitivity and, also, their magnetic properties as the transfer curve offset, and coercivity, for the different stages of irradiation is presented in the following sections.

### 5.2.1 Magneto-transport curves

The magneto-transport curves (transfer curves) of the sensors were obtained with the method mentioned in section 4.4.1. From these characterisations, it is possible to get a first insight into the sensors behaviour and to obtain their characteristic magnetic properties. The transfer curves associated to the

different phases of the experiment of one sample of each group, of the evaluated MR sensors, are represented in Figures 5.2 and 5.3.

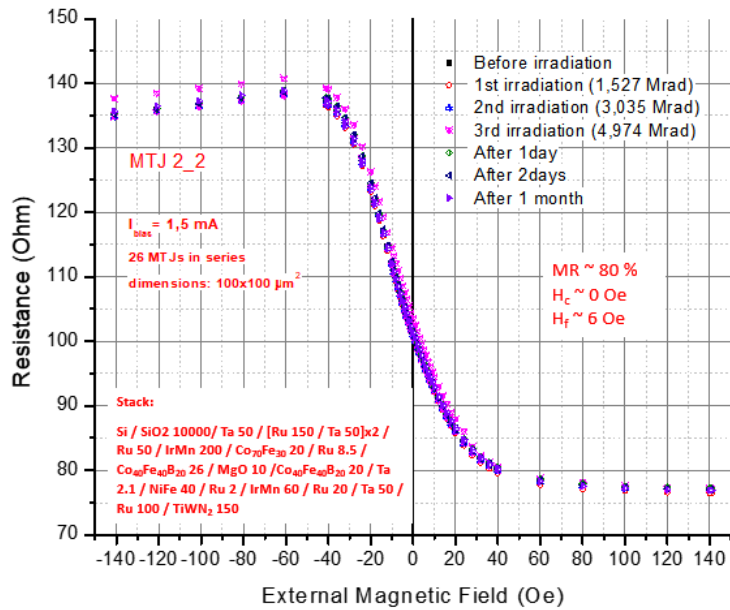


Figure 5.2: Evolution of the transfer curves along the irradiation experiment of a MgO-based MTJ sensor (sample MTJ 2.2). The stack associated to the sensor are identified (from the bottom to the top) by the material of each layer followed by its thickness given in angstroms.

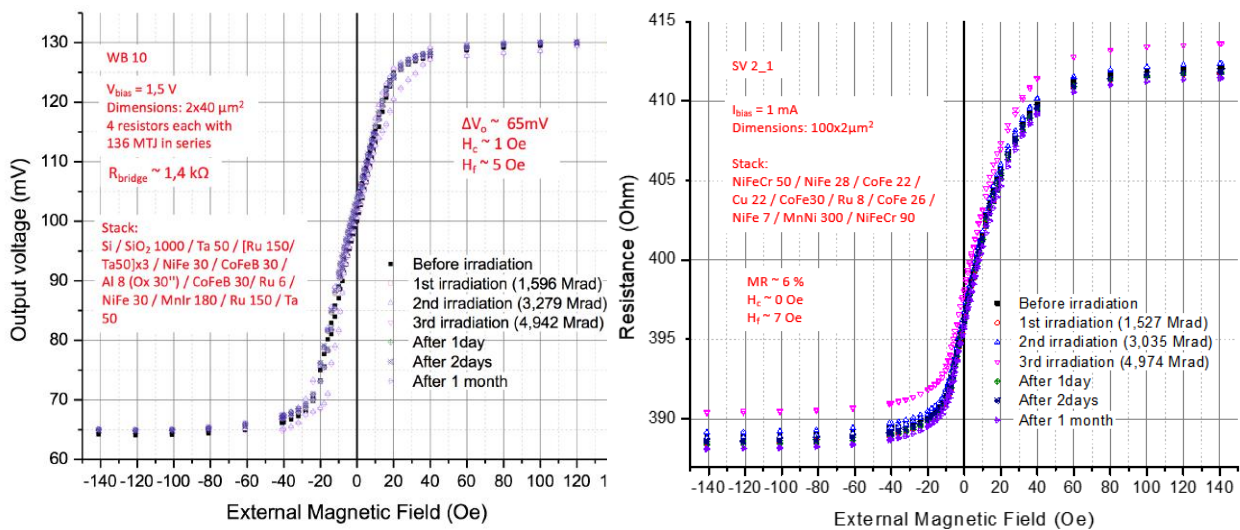


Figure 5.3: Evolution of the transfer curves along the irradiation experiment of (left) Wheatstone bridge with AlOx-based MTJs (sample WB 10), and (right) SV (sample SV 2.2) sensor.

From the global inspection of the evolution of the curves during the irradiation experiment, we see that the sensors still remain functional (a linear response region is observed), and there are no significant modifications on their behaviour after being exposed to a TID of  $\sim 5$  Mrad.

From the transfer curves, we are still able to observe some small variations of the saturated resistances between different curves, and the appearance of some hysterical behaviour (in the transition zones of the WBs curves presented in Figure 5.3 (left)). Nevertheless, these were observed also in the un-irradiated

samples (reference samples) and ended up by being reversed along the experiment.

The resistance variations may be mainly associated with the contacts between the sensors and chip-carrier, as well as with all of the apparatus used to measure the curves (box and connectors). Since the characterisation of the sensors was done remotely, i.e., in a different facility than the ones where they were irradiated, it is suggested that the handling of the sensors may have also caused small modifications in the curves, as well as in other properties analysed in the following sections.

In order to account the handling effects which all of the sensors were submitted, I have used the data of the un-irradiated sample (during the irradiation experiment) and from a test experiment with the same sample, of each group of evaluated MR sensors. The test experiment has consisted on getting data from the un-irradiated sample (about 1 month after the irradiation experiment was done), in order to try to replicate (and so to confirm) the handling conditions that the sensors were submitted to during the irradiation experiment. The data associated to this test was obtained under two distinct situations:

- first I characterised the sample three times by just putting and taking it off from the connector used to measure;
- then, the remain measurements (four) were done after jiggling the sensors (before each measurement) inside of a box.

So, since this data and the one obtained during the irradiation experiment have no relation with gamma irradiation, variations in their values should be only due to handling effects and other external factors, and so, we can compute the uncertainties from these and use them in the data of the irradiated samples in order to have an idea of what variations could have resulted from the handling effects. In order to do this, I took into account the maximum absolute deviation relative to the mean value of some parameter (e.g. for the saturated resistances I have chosen the bigger maximum deviation to the mean value obtained between the two resistance states).

## 5.2.2 Saturated states

Like we saw in the background, the saturated states occur when magnetisations of the FL and the RL are parallel or anti-parallel to each other, translating in a minimum or maximum of electrical resistance identified by the plateaus in the transport curves. The saturated states of the sensors are presented in Figures 5.4, 5.5, and 5.6.

From the inspection of the saturated states we see that:

- for the tree type of sensors evaluated, we see that the parameters correspondent to the saturated states, resistance for the SVs and series of MgO-based MTJs, vary practically within the same interval (band) used to account for the handling effects, with maximum absolute deviations about their mean values of  $R_p$  and  $R_{ap}$  about:  $\sim 2$  and  $\sim 1,5 \Omega$ ,  $\sim 0,3$  and  $\sim 0,8 \Omega$ , respectively. These variations are  $< 1 \%$  relative to the respective  $R_p$  and  $R_{ap}$  mean values;

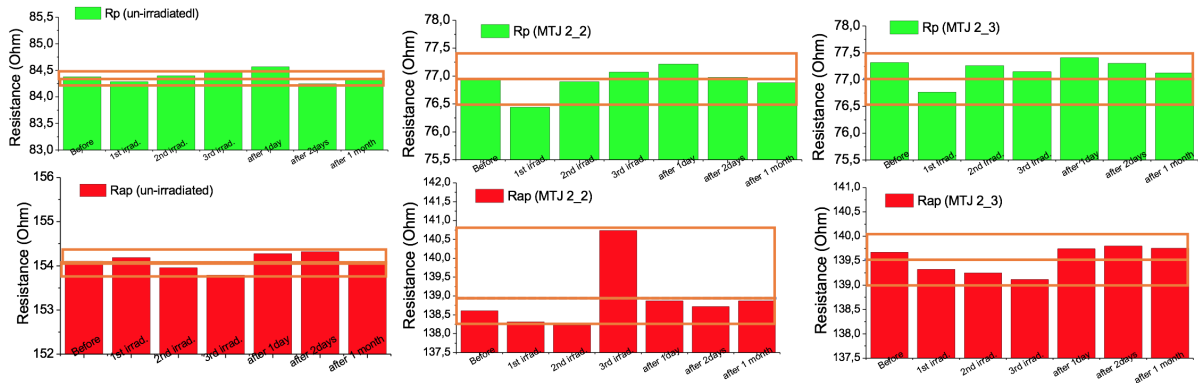


Figure 5.4: Evolution of the saturated states, parallel ( $R_p$ ) and anti-parallel ( $R_{ap}$ ) resistances for the MgO-based MTJs (un-irradiated MTJ, MTJ 2.2 and 2.3) along the irradiation stages. The band represented in each graph represents the interval where variations were observed. These intervals have in consideration the maximum absolute deviations relative to the mean value of  $R_p$  and  $R_{ap}$ , where, for the MgO-based MTJs, maximum deviations of  $\sim 0,3$  and  $\sim 0,8 \Omega$  were, respectively, obtained.

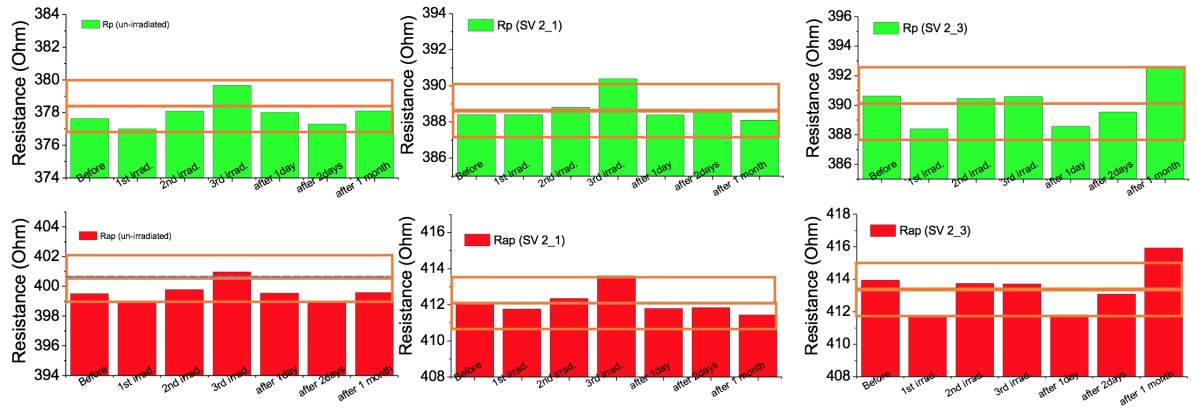


Figure 5.5: Evolution of the saturated states, parallel ( $R_p$ ) and anti-parallel ( $R_{ap}$ ) resistances for the SVs (un-irradiated SV, SV 2.1 and 2.3) along the irradiation stages. The band represented in each graph represents the interval where variations were observed. These intervals were considered to be the maximum absolute deviation relative to the mean value of each sample. For the SVs, the intervals where variations are observed, are associated to maximum absolute deviations of  $\sim 2$  and  $\sim 1,5 \Omega$  relative to  $R_p$  and  $R_{ap}$  mean values, respectively.

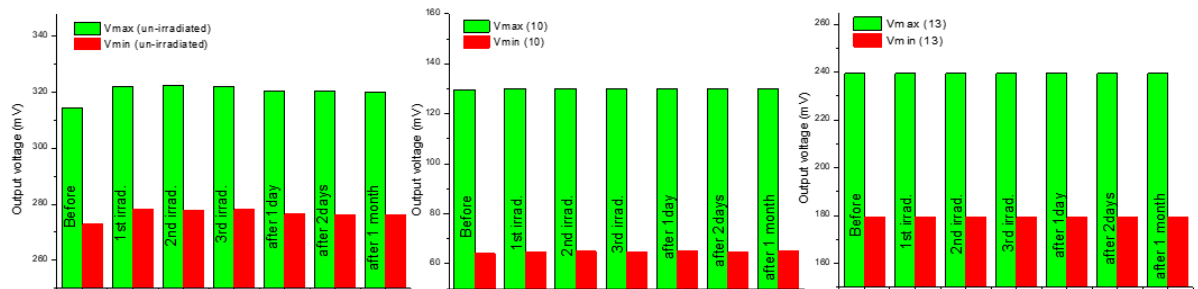


Figure 5.6: Evolution of the saturated voltages,  $V_{min}$  and  $V_{max}$ , for the WBs (un-irradiated WB, WB 10 and 13) along the irradiation stages. For the WBs the variations of the irradiated were considered insignificant (one order below) when compared with the ones verified for the un-irradiated sensor  $\sim 6$  mV for the  $V_{max}$  and  $V_{min}$ .

- for the irradiated WBs we noticed that the intervals where variations have occurred along the experiment were insignificant compared with the one associated to the un-irradiated sample which had a

maximum absolute deviation of  $\sim 6$  mV for the  $V_{max}$  and  $V_{min}$ , considering, so, variations in the irradiated samples (one order below) insignificant;

- for the sample MTJ 2\_2 we noticed a distinguishable superior value of  $R_{ap}$  for the 3rd irradiation phase relative to the values in other phases. Nevertheless, after this phase, the resistance has decreased and remained at the same level during the remain characterisations. This bump in resistance was not verified in any other MTJ sample.

### 5.2.3 MR signal and WB output difference

The output signals of the sensors were also evaluated and are given by the MR ratios of the MTJs and SVs, and by the output difference of the WBs, presented in Figures 5.7, 5.8, and 5.9. Using the same treatment done as before in order to account the effects of handling for the resistances, an interval where the values for the output signals of the irradiated sensors may vary was obtained. Again, in order to obtain the interval where variations occurred, the maximum absolute deviation relative to the mean value of the output signal for each sample was used.

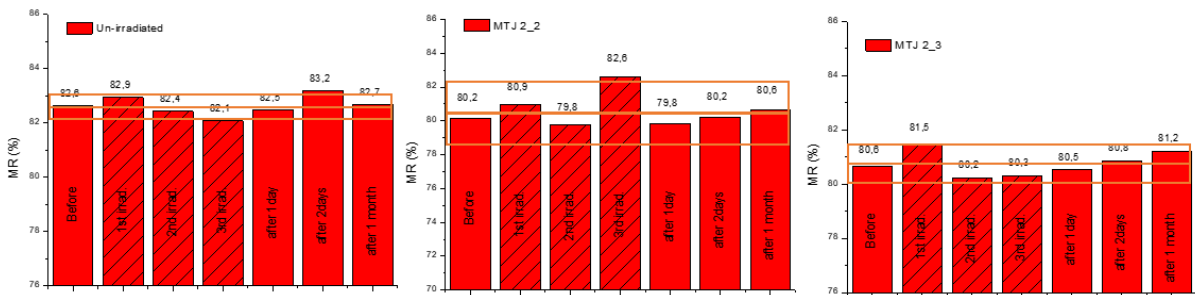


Figure 5.7: Evolution of the MR signal associated to the MgO-based MTJs along the irradiation stages. The bands represented the interval where the variations occurred. For this case, these intervals bands are associated to a maximum absolute deviations close to  $\sim 1,1$  %.

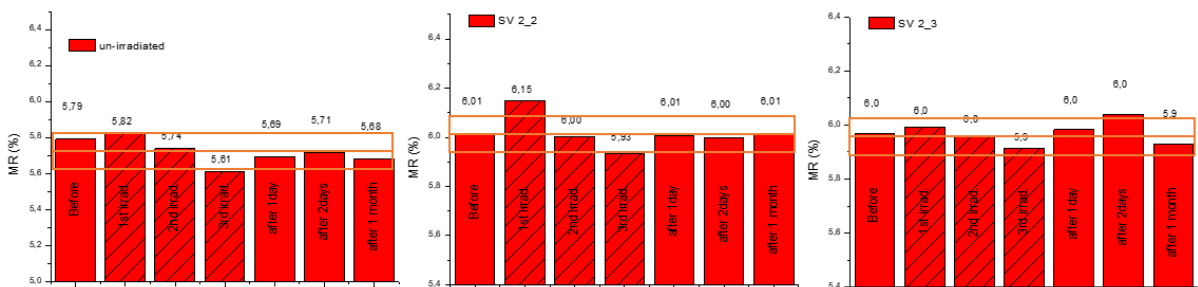


Figure 5.8: Evolution of the MR signal for the SVs along the irradiation stages. For the SVs the intervals where variations were observed, are associated to maximum absolute deviations close to  $0,1$  %.

Like for the saturated states, as we expected, the interval where MR signal variations for the irradiated sensors occurred are practically the same associated to the one observed for the un-irradiated sample, as we may see in the Figures 5.7 and 5.8.

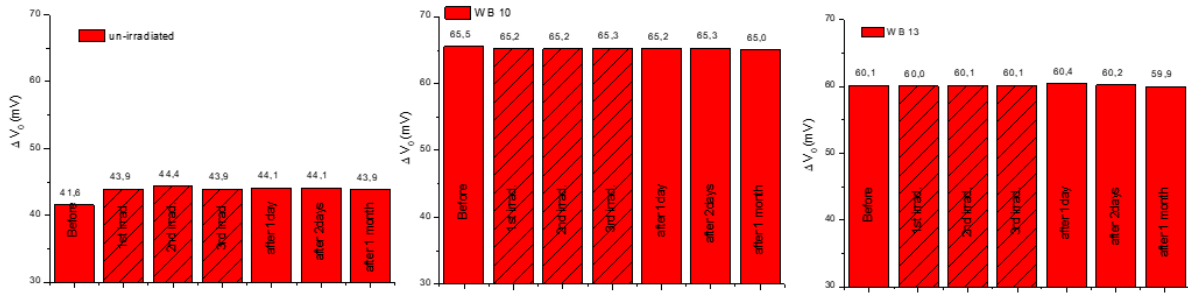


Figure 5.9: Evolution of the output signal,  $\Delta V_0 = V_{max} - V_{min}$ , for the WBs along the irradiation stages.

## 5.2.4 Coercivity

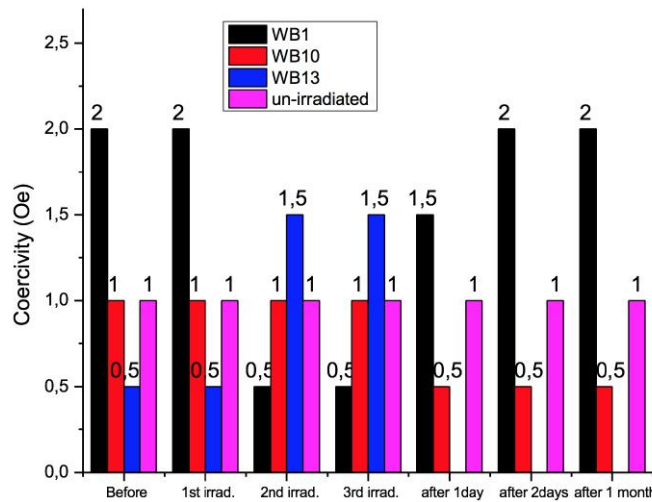


Figure 5.10: Coercivity evolution for the WBs (un-irradiated WB, WB 1, 10 and 13) along the irradiation stages.

Coercivity of a sensors can be defined as the hysteretic behaviour close to zero field. For this region, the data was obtained with a step of 1 Oe. So the obtained data for the coercivity field as an uncertainty of 0,5 Oe for this region.

The MgO-based MTJ and SV irradiated sensors presented, practically, no coercivity. For the WBs we saw that some 1,5 Oe variations for the WB 1 and 13, as we can see in Figure 5.10. Nevertheless, for the three evaluated sensors no trend associated to irradiation was verified, what suggest us that, probably, these variations are not related with irradiations, but maybe with some intrinsic behaviour.

## 5.2.5 Transfer curve offset relative to zero field

The shift of the curves (which corresponds to the field of the middle-point of a curve) was another evaluated parameter and the results are presented in Figures 5.11. Shifts in transfer curves may result from an effective coupling field as a consequence from the interactions between the magnetic layers, like, ferromagnetic Néel coupling between the FM layers separated by a spacer (FM / spacer / FM) induced from interface interactions, the coupling of the demagnetizing field of both FM layers, and the exchange

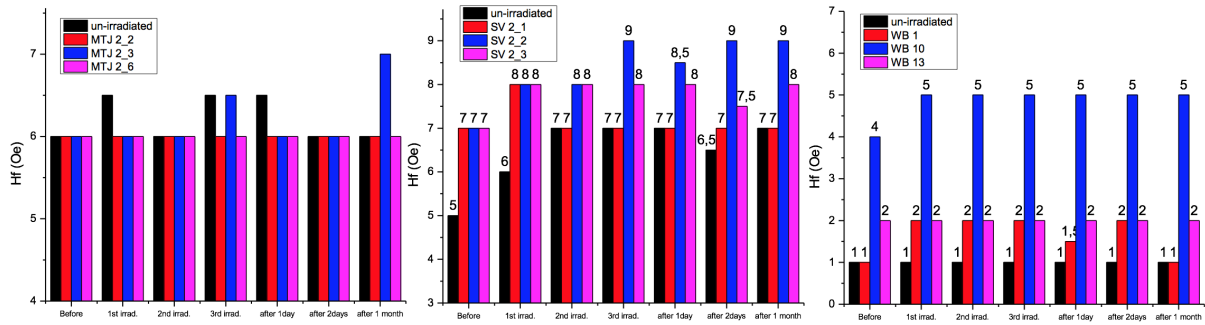


Figure 5.11: Evolution of the transfer curve offset for (left) MgO-based MTJs, (middle) SVs, and (right) WBs along the irradiation stages.

coupling across the spacer described by RKKY-theory (where depending on the spacer thickness a ferromagnetic/antiferromagnetic exchange coupling between the FM layers may occur).

From the inspection of this parameter, we may also consider that gamma irradiation did not have any relevant effect, since the variations occurred in the irradiated samples have practically the same magnitude as the uncertainty associated to the field (0,5 Oe for the 1 Oe step field).

## 5.2.6 Sensitivity

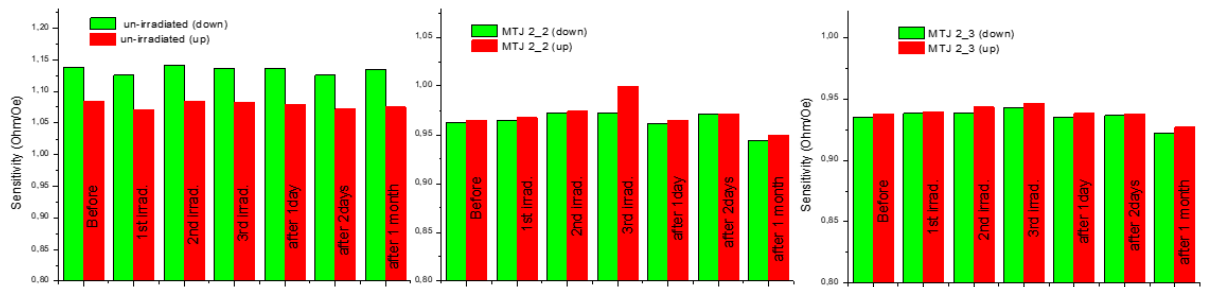


Figure 5.12: Evolution of the sensitivity of the MgO-based MTJs along the irradiation stages.

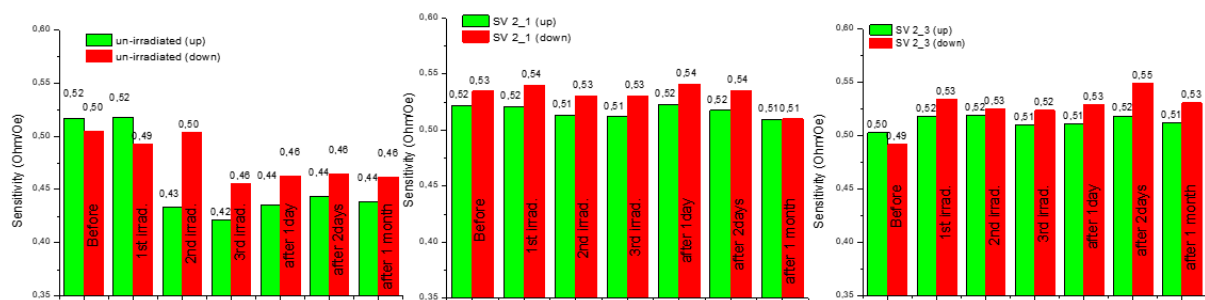


Figure 5.13: Evolution of the sensitivity of the SVs along the irradiation stages.

In order to evaluate the sensitivity of the sensors, linear fittings of the transfer curves in a region close to zero field (field range between -10 Oe to 10 Oe) where the data were more precisely obtained (with field steps of 1 Oe) were done. Sensitivities are presented in Figures 5.12, 5.13 and 5.14, and they reflect the

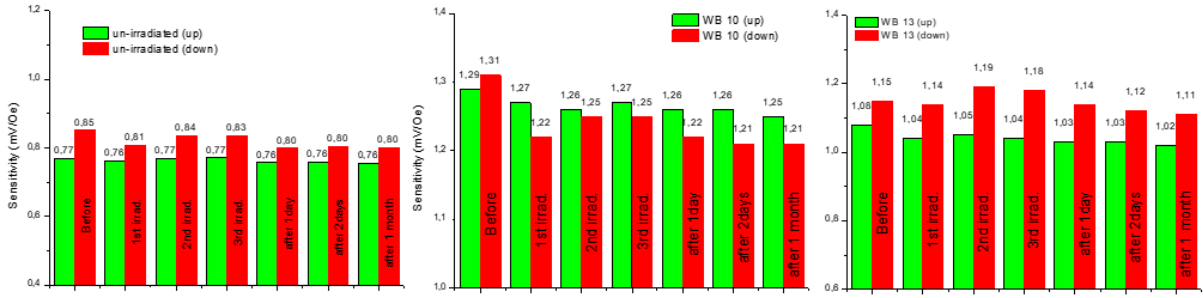


Figure 5.14: Evolution of the sensitivities of the WBs along the irradiation stages.

rotation of the free layer as the field is changing. The sensitivities were obtained for the two directions along in which the field varied, and are denominated by up and down.

For sensitivity, the results practically do not show any significant variations or trend indicative of irradiations effects. The small variations observed (of the order of 0,01 mV/Oe) are due other external factors like the handling of the sensors.

## Chapter 6

# Conclusions

From the analysis of the data presented in section 5.2, no tested sample was found to suffer any relevant degradation due to irradiation with  $^{60}\text{Co}$  gammas. The sensors kept their global performance intact, like we observed in the transfer curves, during the irradiation experiment. Some of these curves have shown some changes, like variations of resistance and, also, the appearance of the hysteresis-like behaviour. Nevertheless, these changes were reversed. About the origin of these changes, it was concluded that they did not have anything to do with the irradiation since:

- through the inspection of the magneto-transport and sensor parameters (coercivity, curve offset, MR signal, saturated states, and sensitivity) we observed that, for the three types of evaluated sensors, though some of them had felt small variations, no explicit trend showing any sign of potential gamma irradiation damage during the characterisations was observed neither within each group of sensors nor among the four types;
- another aspect that may support the conclusion that the sensors did not suffer measurable damage, comes from the comparison of the irradiated sensors with the non-irradiated ones (reference samples). The small changes which were verified in the irradiated sensors were also equally verified in the reference samples, being in some cases even higher in these sensors;

From these two main points, we conclude that many of these changes have resulted from other external factors (mainly the handling of the sensors) which were not related with the irradiations, factors that were felt by the irradiated and non-irradiated samples. The fact that the sensors were not measured at the same place where they were irradiated played an important role in the observed changes. In order to try to replicate the conditions that the reference as well as the irradiated samples were subjected to during the irradiation experiment, a simple test was performed with the reference ones, trying to repeatedly replicate the handling of all sensors. Even the conditions, in order to try to repeat the control results were not the same, it was possible to observe from the test results that in some of the cases the inspected parameters suffered variations with magnitudes higher than the ones observed in the variations verified for the irradiated sensors. These just support our suggestion that sensor handling factor might have

been the main responsible for the small observed changes in the behaviour of the sensors, and not the irradiation to which they were exposed. In order to mitigate the type of variations in future experiments, characterisations should be done at the irradiation facility.

So, due to these facts and also due to the fact that no concrete and well distinguishable signal of radiation effect was actually noticed, we observed that for the inspected range, the evaluated magnetoresistive sensors (SVs, MgO-based MTJs and AlOx-based MTJs in a Wheatstone bridge configuration) are resistant to high total ionizing doses as expected and also showed in previous works [4, 5], which make these type of magnetic sensors desired to be used for space applications, at least in terms of radiation tolerance. This high tolerance to radiation comes from the fact that the gammas have so high energies that they may pass through the materials without interacting with them, and/or, because ionizing radiation will not affect the mechanism which these sensors are based on which is related with spin transport (which seems not to be influenced by the radiation) when not only a voltage, but also a magnetic field are applied.

# Bibliography

- [1] M. Díaz-Michelena, "Small magnetic sensors for space applications," *Sensors*, vol. 9, no. 4, pp. 2271–2288, 2009.
- [2] R. Bamford, B. Kellett, W. Bradford, C. Norberg, A. Thornton, K. Gibson, I. Crawford, L. Silva, L. Gargaté, and R. Bingham, "Minimagnetospheres above the lunar surface and the formation of lunar swirls," *Physical review letters*, vol. 109, no. 8, p. 081101, 2012.
- [3] R. Slatter, "Magnetoresistive (mr) sensors for angle-, path-and current measurement in harsh environments," in *17 th International Conference on Sensors and Measurement Technology, Nürnberg*, 2015.
- [4] N. Anuniwat, *Radiation Effects on Magnetic Tunnel Junctions and Novel Magnetic thin Films*. PhD thesis, Faculty of the School of Arts and Sciences, University of Virginia, 2015.
- [5] F. Ren, "Radiation Tolerance of Magnetic Tunnel Junctions with MgO Barriers," Master's thesis, Oregon State University, 2012.
- [6] P. P. Freitas, R. Ferreira, and S. Cardoso, "Spintronic sensors," *Proceedings of the IEEE*, vol. 104, no. 10, pp. 1894–1918, 2016.
- [7] A. N. V. da Silva, *Towards sub-100nm Magnetoresistive Devices: From Simulations to Applications*. PhD thesis, Instituto Superior Técnico, Universidade de Lisboa, 2016.
- [8] W. Thomson, "On the electro-dynamic qualities of metals:—effects of magnetization on the electric conductivity of nickel and of iron," *Proceedings of the Royal Society of London*, vol. 8, pp. 546–550, 1856.
- [9] R. Sanz, A. B. Fernández, J. A. Dominguez, B. Martín, and M. D. Michelena, "Gamma irradiation of magnetoresistive sensors for planetary exploration," *Sensors*, vol. 12, no. 4, pp. 4447–4465, 2012.
- [10] T. McGuire and R. Potter, "Anisotropic magnetoresistance in ferromagnetic 3d alloys," *IEEE Transactions on Magnetics*, vol. 11, no. 4, pp. 1018–1038, 1975.
- [11] A. Persson, *Magnetoresistance and Space : Micro- and Nanofeature Sensors Designed, Manufactured and Evaluated for Space Magnetic Field Investigations*. PhD thesis, Faculty of Science and Technology, Uppsala University, 2011.

- [12] P. Ribeiro, "Ciliary structure inspired force sensor for robotic platforms," Master's thesis, Instituto Superior Técnico, Universidade Lisboa, 2016.
- [13] M. N. Baibich, J. M. Broto, A. Fert, F. N. Van Dau, F. Petroff, P. Etienne, G. Creuzet, A. Friederich, and J. Chazelas, "Giant magnetoresistance of (001) fe/(001) cr magnetic superlattices," *Physical review letters*, vol. 61, no. 21, p. 2472, 1988.
- [14] B. Dieny, "Spin valves," in *Magnetoelectronics* (M. Johnson, ed.), ch. 2, pp. 67–150, Elsevier, 2004.
- [15] P. Freitas, R. Ferreira, S. Cardoso, and F. Cardoso, "Magnetoresistive sensors," *Journal of Physics: Condensed Matter*, vol. 19, no. 16, p. 165221, 2007.
- [16] J. S. Moodera and R. H. Meservey, "Spin-polarized tunneling," in *Magnetoelectronics* (M. Johnson, ed.), ch. 3, pp. 151–378, Elsevier, 2004.
- [17] F. Franco, "High Sensitivity Magnetoresistive Based Systems for Non-Destructive Testing (NDT) Applications," Master's thesis, Instituto Superior Técnico, Universidade Lisboa, 2014.
- [18] G. Farinha, "Compact size 3D magnetometer based on magnetoresistive sensors," Master's thesis, Instituto Superior Técnico, Universidade Lisboa, 2015.
- [19] S. I. R. Arias, D. R. Muñoz, S. Cardoso, R. Ferreira, and P. J. P. de Freitas, "Total ionizing dose (tid) evaluation of magnetic tunnel junction (mtj) current sensors," *Sensors and Actuators A: Physical*, vol. 225, pp. 119–127, 2015.
- [20] A. Lopes, "MgO Magnetic Tunnel Junction sensors in Full Wheatstone bridge conguration for Electrical Current detection," Master's thesis, Instituto Superior Técnico, Universidade Lisboa, 2012.
- [21] E. Benton and E. Benton, "Space radiation dosimetry in low-earth orbit and beyond," *Nuclear Instruments and Methods in Physics Research Section B: Beam Interactions with Materials and Atoms*, vol. 184, no. 1, pp. 255–294, 2001.
- [22] M. A. Xapsos, P. M. O'Neill, and T. P. O'Brien, "Near-earth space radiation models," *IEEE Transactions on Nuclear Science*, vol. 60, no. 3, pp. 1691–1705, 2013.
- [23] C. Patrignani, D. Weinberg, C. Woody, R. Chivukula, O. Buchmueller, Y. V. Kuyanov, E. Blucher, S. Willocq, A. Höcker, C. Lippmann, *et al.*, "Review of particle physics," *Chin. Phys.*, vol. 40, p. 100001, 2016.
- [24] P. A. Cassak, *Catastrophe model for the onset of fast magnetic reconnection*. PhD thesis, University of Maryland.
- [25] F. B. McLean and T. R. Oldham, "Basic mechanisms of radiation effects in electronic materials and devices," tech. rep., HARRY DIAMOND LABS ADELPHI MD, 1987.
- [26] N. Saks and D. Brown, "Interface trap formation via the two-stage h/sup+/process," *IEEE Transactions on Nuclear Science*, vol. 36, no. 6, pp. 1848–1857, 1989.

- [27] J. Srour, C. J. Marshall, and P. W. Marshall, "Review of displacement damage effects in silicon devices," *IEEE Transactions on Nuclear Science*, vol. 50, no. 3, pp. 653–670, 2003.
- [28] D. Gordon and R. Sery, "Effects of charged particles and neutrons on magnetic materials," *IEEE Transactions on Communication and Electronics*, vol. 83, no. 73, pp. 357–361, 1964.
- [29] A. Tench and M. Duck, "Radiation damage in oxides. i. defect formation in mgo," *Journal of Physics C: Solid State Physics*, vol. 6, no. 7, p. 1134, 1973.
- [30] Z. Guo, D. You, J. Qiu, K. Li, and Y. Wu, "Influence of  $ga^+$  ion irradiation on magnetoresistance and exchange bias of irmn/cofe/cu/cofe/nife spin valve," *Solid state communications*, vol. 120, no. 11, pp. 459–462, 2001.
- [31] T. K. Carroll, "Radiation Damage in GMR Spin Valves," Master's thesis, Ohio State University, 2010.
- [32] Y. Conraux, J. Nozieres, V. Da Costa, M. Toulemonde, and K. Ounadjela, "Effects of swift heavy ion bombardment on magnetic tunnel junction functional properties," *Journal of applied physics*, vol. 93, no. 10, pp. 7301–7303, 2003.
- [33] Y. Han, S. Kim, S. Lee, J. Hong, D. R. Lee, H. H. Lee, Y. J. Park, and H. Lee, "Effects of h-ion irradiation on the properties of a spin valve," *Journal of Applied Physics*, vol. 103, no. 7, p. 07B521, 2008.
- [34] J. Lu, S. J. Poon, S. A. Wolf, B. D. Weaver, P. J. McMarr, H. Hughes, and E. Chen, "Radiation effects on the magnetism and the spin dependent transport in magnetic materials and nanostructures for spintronic applications," *Journal of Materials Research*, vol. 30, no. 9, pp. 1430–1439, 2015.
- [35] L. Rosado, F. Cardoso, F. Franco, R. Ferreira, E. Paz, S. Cardoso, P. Ramos, P. Freitas, and M. Piedade, "Detection of micrometric surface defects in titanium using magnetic tunnel junction sensors," in *Proceedings of the 11th European Conference on Non-Destructive Testing (EC-NDT'14)*, 2014.



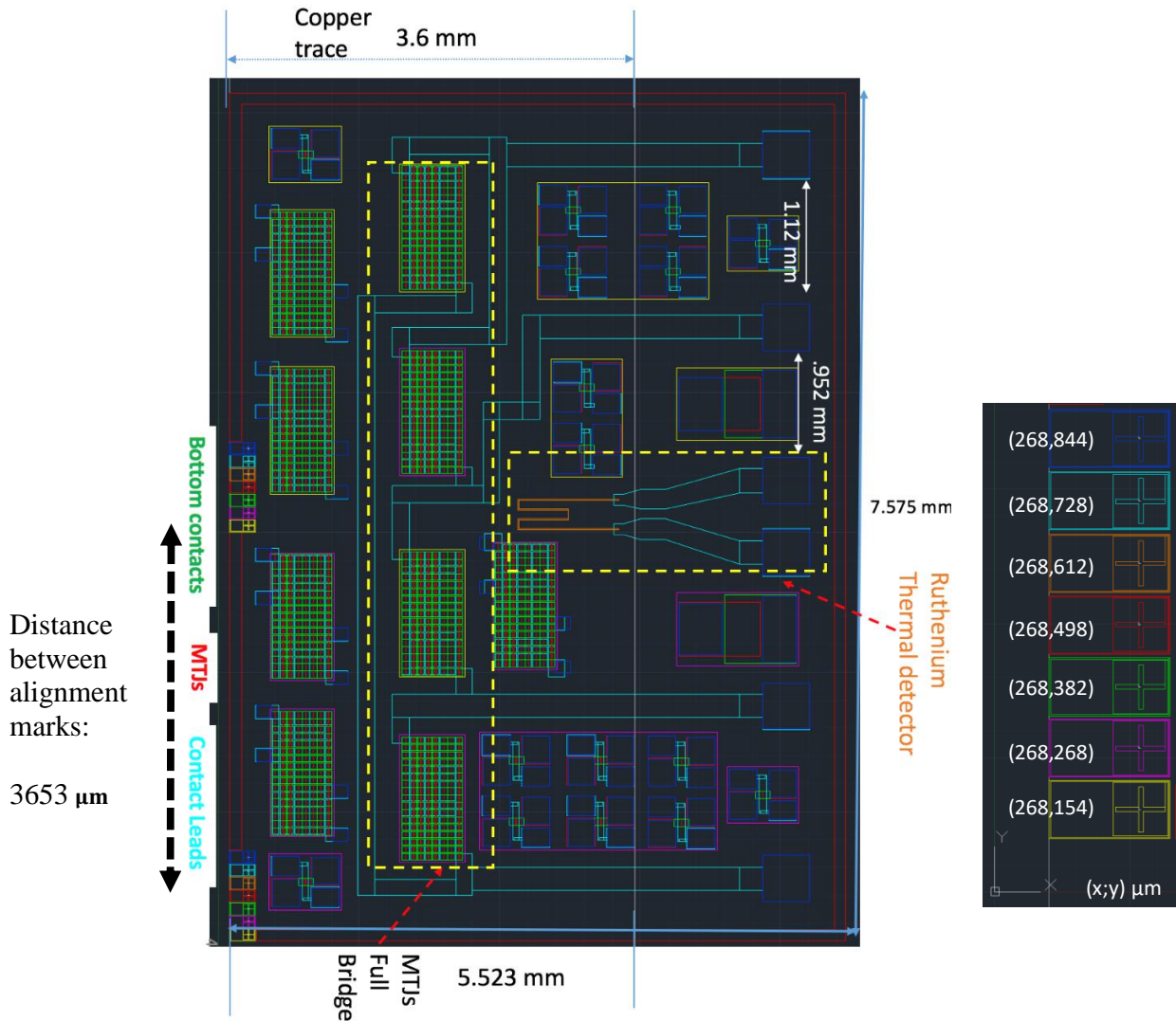
## **Appendix A**

# **Run-sheet - Current sensors**

## Run Sheet - Current sensors

Current Sensors, based on TMR effect, in a Full Wheatstone bridge configuration

Autocad design:



Mask	1st exposure	2nd	3rd	4th	5h	6th	7th
	Block1	Block2	Bottom electrodes	MTJ column	Ru Temp. sensor	Top electrode	Vias
cs	csl1	csl2	csl3	csl4	csl5	csl6	csl7

➤ **Step 1: 1<sup>st</sup> Exposure – Blocks definition for MTJ stack deposition**

1) Vapor Prime 30 min (**Recipe - 0**):

2) Coat 1.5 μm PR (**Recipe 6/2**)

1. Dispense photoresist on the sample and spinning at 800 rpm for 5 sec.
2. Spin at 2500 rpm for 30 sec. to obtain ~1.45μm thickness.
3. Soft bake at 85°C for 60 seconds

Step description	Conditions
Wafer dehydration	Vacuum, 10 Torr, 2 min. N2 inlet, 760 Torr, 3 min. Heating to 130°C
Priming	Vacuum, 1 Torr, 3 min. HDMS, 6 Torr, 5 min.
Purge prime exhaust	Vacuum, 4 Torr, 1 min. N2 inlet, 500 Torr, 2 min. Vacuum, 4 Torr, 2 min.
Return to atmosphere	N2 inlet, 3 min.

3) Lithography – Machine: DWL

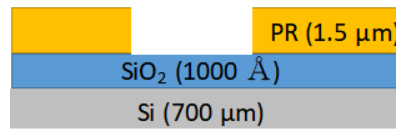
**MAP:** CSNEW  
**Energy:** 75 %

**Mask:** csl1 (non-inverted)  
**Power:** 90 mW

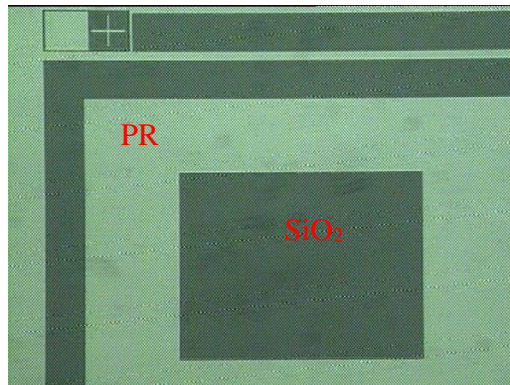
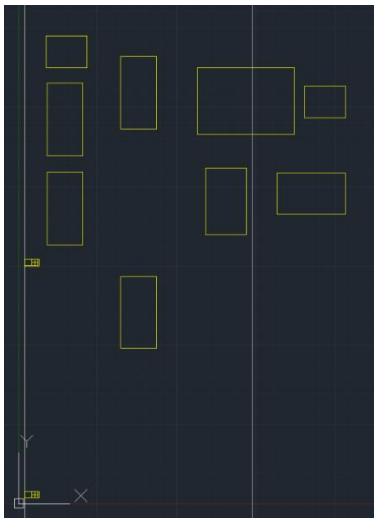
**Origin:** (3600;5700) μm  
**Focus:** +30

4) Development (**Recipe 6/2**)

1. Bake at 110°C for 60s
2. Cool for 30s
3. Developer (TMA238WA) for 60s



5) Observations:



➤ **Step 2: Deposition MTJ1 stack (AlOx barrier)**

**Attention: Take note of M orientation on the wafer**

<b>Machine:</b> Nordiko 3000	<b>BP:</b> $7.7 \times 10^{-7}$ Torr
<b>Batch:</b> AlOx_one	<b>Recipe:</b>

**Sample:** TJ2063

**Stack** (1164 Å): Ta 50 / [Ru 150/ Ta50]x3 / NiFe 30 / CoFeB 30 / Al 8 (Ox 30") / CoFeB 30/ Ru 6 / NiFe 30 / MnIr 180 / Ru 150 / Ta 50 (thickness in Å)



**Standard values:**

110W / +1022V/ -300V/ 24mA/ 1.7sccm  
100W / 710V/ -300V/ 24mA/ 1.7sccm (alumina)

**Deposition read values:**

127W / 1001V / 24.3mA / -292.5V / 0.8mA / 1.7sccm / 50% / 80°  
109W / 3.9 sccm Ar / 8x5 sccm O2 / 13.5V / 0.4mA / 0V / 2.9mA (oxidation)  
88W / 695V / 15.2mA / -292V / 0.8mA / 1.7sccm (Al deposition)

➤ **Step 3: Lift-off of the 1<sup>st</sup> MTJ stack**

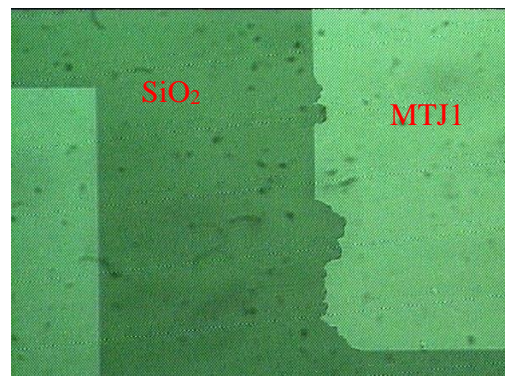
**Sample:** TJ2063

1) Hot Micro-Strip (65°C) + Ultrasounds

2) Rinse with IPA + DI water + dry compressed air

**Observations:**

- After the lift-off, it was noticed that some of the material was not deposited properly at the Si/SiO<sub>2</sub> substrate. The reason for this was that the substrate was not well clean. For the next MTJ2 deposition, do first an etch step to clean the substrate before depositing the material.



➤ **Step 4: 2<sup>nd</sup> Exposure – Blocks definition for MTJ stack deposition**

Sample: TJ2063

1) Vapor Prime 30 min (Recipe - 0)

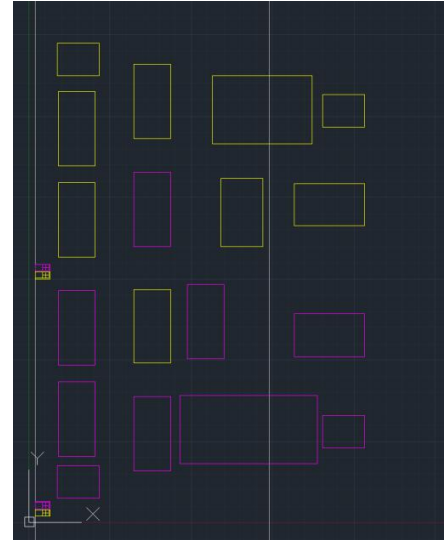
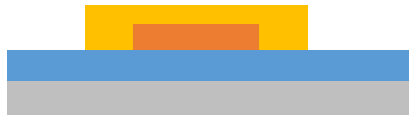
2) Coat 1.5 μm PR (Recipe 6/2)

3) Lithography – Machine: DWL

MAP: CSNEW                      Mask: csl2 (non-inverted)  
Energy: 55 %                      Power: 90 mW  
Focus: +30                          Origin: (268;154) μm

4) Development (Recipe 6/2)

Observations:



➤ **Step 5: Deposition MTJ2 stack (AlOx barrier)**

Sample: TJ2063

**Attention: Rotate the sample 180° in order to have oppose M**

Also, clean first the substrate by doing 1 minute of etching  
- (etch\_70pan\_60s)

<b>Machine:</b> Nordiko 3000	<b>BP:</b>
<b>Batch:</b> AlOx_one	<b>Recipe:</b>

Sample: TJ2068 (deposited)

**Stack** (1164 Å): Ta 50 / [Ru 150/ Ta50]x3 / NiFe 30 / CoFeB 30 / Al 8 (Ox 30") / CoFeB 30 / Ru 6 / NiFe 30 / MnIr 180 / Ru 150 / Ta 50 (thickness in Å)

**Standard values:**

110W / +1022V/ -300V/ 24mA/ 1.7sccm  
100W / 710V/ -300V/ 24mA/ 1.7sccm (alumina)

**Deposition read values:**

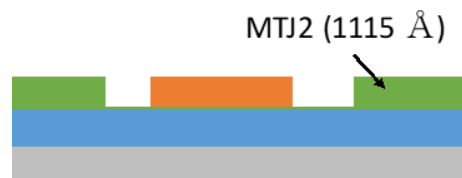
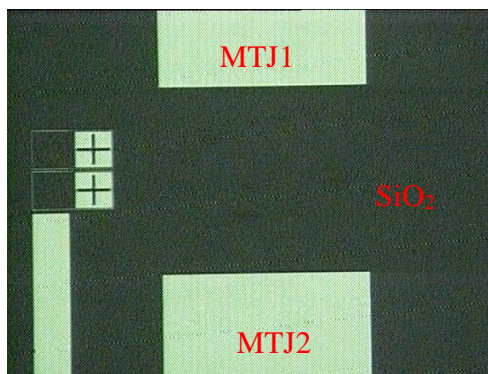
129W / 1000.5V / 24.1mA / -292.3V / 0.8mA / 1.7sccm / 50% / 80°  
109W / 3.9 sccm Ar / 8x5 sccm O2 / 12.3V / 0.4mA / 0V / 2.9mA (oxidation)  
87W / 694.9V / 14.9mA / -292.3V / 0.8mA / 1.6sccm (Al deposition)

➤ **Step 6: Lift-off of the 2<sup>nd</sup> MTJ stack**

Sample: TJ2063/68

- 1) Hot Micro-Strip (65°C) + Ultrasounds
- 2) Rinse with IPA + DI water + dry compressed air

**Observations:**



➤ **Step 7: 3<sup>rd</sup> Exposure – Bottom electrodes definition**

Sample: TJ2063/68

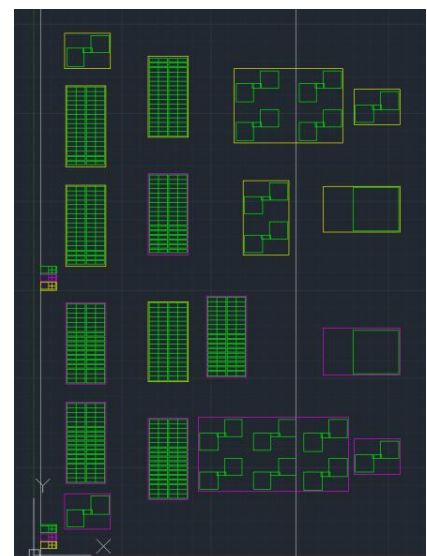
- 1) Vapor Prime 30 min (Recipe - 0):
- 2) Coat 1.5 μm PR (Recipe 6/2)
- 3) Lithography – Machine: DWL

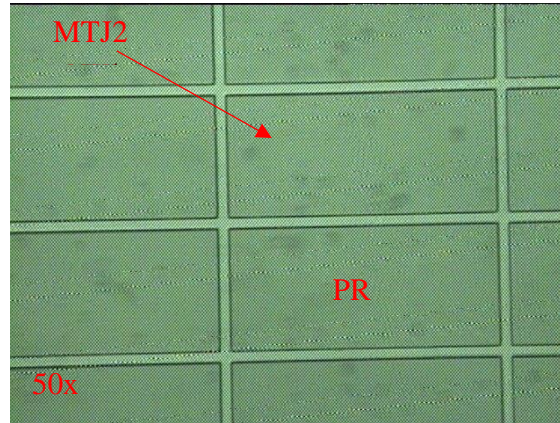
MAP: CSNEW	Mask: csl3 (inverted)
Energy: 55 %	Power: 100 mW
Focus: 0	Origin: (268;154) μm

- 4) Development (Recipe 6/2)

**Observations:**

- The PR may not be removed from structures associated with the resistors of the bridge by just doing 60 seconds of development. Do it until a good level of cleanness has been obtained in order to have a well definition and no short circuits in the bottom contacts after the next etching step.





➤ **Step 8: 1<sup>st</sup> Ion milling – bottom electrode shape definition**

Sample: TJ2063/68

Machine: Nordiko 3000      BP:  $8.2 \times 10^{-7}$  Torr  
Batch: junction\_etch

Total thickness to etch: 1164 Å

Etch Rate: 1 Å/s → Time = 1207 ” @ 70°

Standard Etching Recipe: vac\_wait / etch\_gun\_stab\_70pan / junction\_etch\_70pan / end\_etch

Assist Gun standard values: 54W/ 500V/-200V, 30mA, 8sccm Ar; 40rpm

Assist Gun	Power (W)	V+ (V)	I+ (mA)	V- (V)	I- (mA)	Ar Flux (sccm)	Pan (°)	Rotation (%)
Read Values	53	488.3	27.8	194.3	1.6	7.9	70	40

**Observations:**

- DO NOT OVERETCH, to avoid to reach the Si layer in the next etching process (etch junctions)

➤ **Step 9: Resist strip**

- 1) Hot Micro-Strip (65°C) + Ultrasounds
- 2) Rinse with IPA + DI water + dry compressed air

**Observations:**

➤ **Step 10: 4<sup>th</sup> Exposure – MTJ pillars**

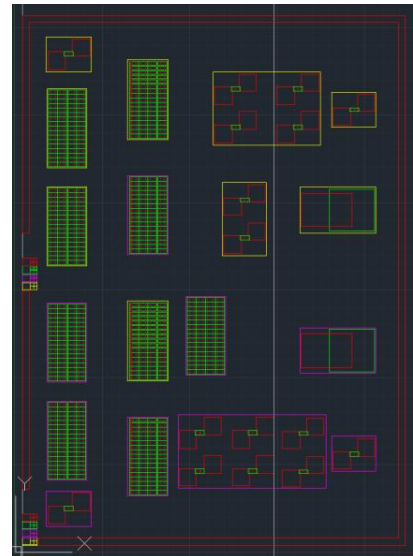
Sample: TJ2063/68

- 1) Vapor Prime 30 min (Recipe - 0):
- 2) Coat 1.5 µm PR (Recipe 6/2)
- 3) Lithography – Machine: DWL

MAP: CSNEW                      Mask: csl4 (*inverted*)  
Energy: 55 %                    Power: 100 mW  
Focus: 0                            Origin: (268;154) µm

- 4) Development (Recipe 6/2)

**Observations:**



- Check the MTJ pillar dimensions! (expected dimension 2x40 µm<sup>2</sup>)

➤ **Step 11: 2<sup>nd</sup> Ion milling – MTJ pillar**

Sample:  
TJ2063/68

Machine: Nordiko 3000

BP:

Batch: etch

Total thickness to etch: 564 Å = 454 Å @ 70° + 110 Å @ 40°

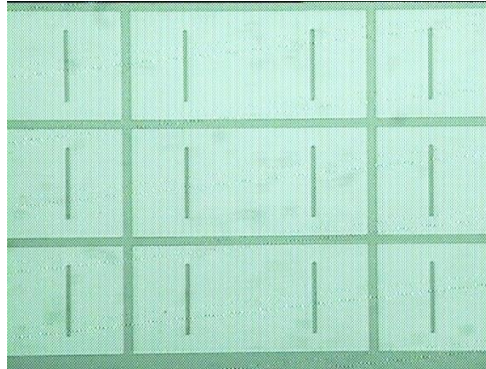
Etch Rates: 1 Å/s (@70) and 0.654 Å/s (@40) → Time = 575''@70° + 180'' @40°  
(with overetch included)

Standard Etching Recipe: vac\_wait / etch\_gun\_stab\_70pan / junction\_etch\_70pan /  
vac\_wait / / etch\_gun\_stab\_40pan / junction\_etch\_40pan / end\_etch

Assist Gun standard values: 54W/ 500V/-200V, 30mA, 8sccm Ar; 40rpm

Assist Gun	Power (W)	V+ (V)	I+ (mA)	V- (V)	I- (mA)	Ar Flux (sccm)	Pan (°)	Rotation (%)
Read Values							70 and 40	40

**Observations:**



➤ **Step 12: 1<sup>st</sup> passivation - deposition of alumina (Al<sub>2</sub>O<sub>3</sub>)**

Sample: TJ2063/68

Machine: UHV2

BP: 8.7x10<sup>-7</sup> Torr

Expected thickness:

1300 Å

	Deposition Time	Al <sub>2</sub> O <sub>3</sub> thickness	Ar gas flow	Pressure	Power Source	Frequency
Read	1h45 min	1214 Å	45 sccm	1.6 mTorr	200 W	544 Hz

➤ **Step 13: Oxide lift-off**

Sample: TJ2063/68

1) Hot Micro-Strip (65°C) + Ultrasounds

2) Rinse with IPA + DI water + dry compressed air

**Observations:**

➤ **Step 14: 5<sup>th</sup> Exposure – Ru temperature sensor definition**

Sample: TJ2063/68

1) Vapor Prime 30 min (Recipe - 0):

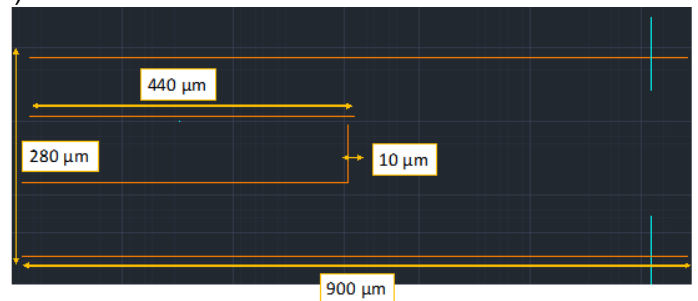
2) Coat 1.5 μm PR (Recipe 6/2)

3) Lithography – Machine: DWL

MAP: CSNEW      Mask: csl5 (non-inverted)  
Energy: 55 %      Power: 100 m  
Focus: 0          Origin: (268;154) μm

4) Development (Recipe 6/2)

Observations:



➤ **Step 15: Deposition of Ru temperature sensor**

Sample: TJ2063/68

**Machine:** Nordiko 2000  
**Batch:** function test

**BP:**  $8.1 \times 10^{-8}$  Torr  
**Recipe:** T3Ta 50 / T2Ru 400

**Materials:** Ta 50 Å / Ru 400 Å

Ar flow: 10 sccm (for Ta deposition); Ar flow: 8 sccm (for Ru deposition)

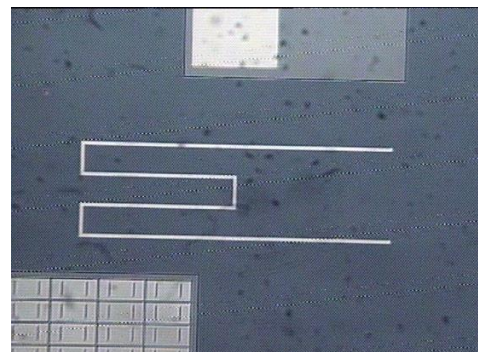
➤ **Step 16: Lift-off**

Sample: TJ2063/68

1) Hot Micro-Strip (65°C) + Ultrasounds

2) Rinse with IPA + DI water + dry compressed air

Observations:



➤ **Step 17: 6<sup>th</sup> Exposure – Top electrodes definition**

Sample: TJ2063/68

1) Vapor Prime 30 min (Recipe - 0):

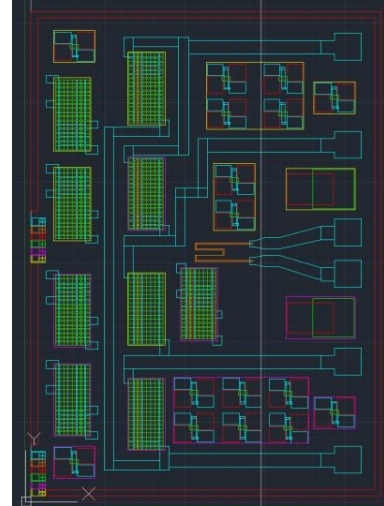
2) Coat 1.5 μm PR (Recipe 6/2)

3) **Pre-development (manually)**

1. Developer (TMA238WA) for 20s

4) Lithography – Machine: DWL

MAP: CSNEW                      Mask: csl6 (**non-inverted**)  
 Energy: 55% + 25%          Power: 100 mW  
 Focus: 0                              Origin: (268;154) μm



5) Development (Recipe 6/2)

Observations:

- **die 18**: the PR was not completely removed from the structures where was supposed to deposit AlSiCu, even after developing the sample during 1 min + 4x10s extra development.



➤ **Step 18: AlSiCu deposition (top electrodes)**

Sample: TJ2063/68

Machine: Nordiko 7000                      Seq. Metalization 1.2um low power

Thickness to deposit: 4 x 3000 Å AlSiCu + (27'') TiWN<sub>2</sub>

Sequence: Soft Sputter Etch 60'' + 4 x 320'' (AlSiCu dep.) + 4x250'' cool\_downs + 27'' (TiWN<sub>2</sub> dep.)

Readings – Module 2 (Soft Sputter Etch)				
Run#	Power1 (W)	Power2 (W)	Gas flux (sccm)	Pressure (mTorr)
		60		3
Readings – Module 4 (AlSiCu deposition)				
Run#	Power1 (kW)	Target V and I	Gas flux (sccm)	Pressure (mTorr)
	0.48	349 V; 1.48 A	49.9	3.6

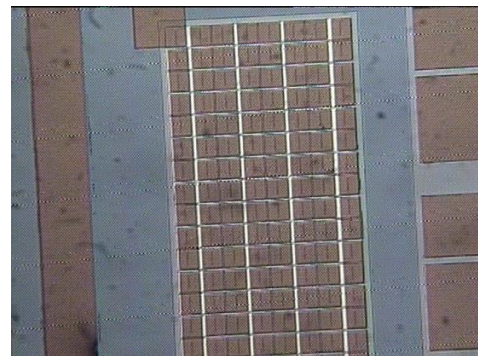
Readings – Module 3 (TiWN <sub>2</sub> deposition)				
Run#	Power1 (kW)	Power2 (W)	Gas flux 1 and 2 (sccm)	Pressure (mTorr)
	0.5		49.8 ; 9.8	3.0

➤ **Step 19: AlSiCu lift-off**

Sample: TJ2063/68

- 1) Hot Micro-Strip (65°C) + Ultrasounds
- 2) Rinse with IPA + DI water + dry compressed air

**Observations:**



➤ **Step 20: 7<sup>th</sup> Exposure - Vias**

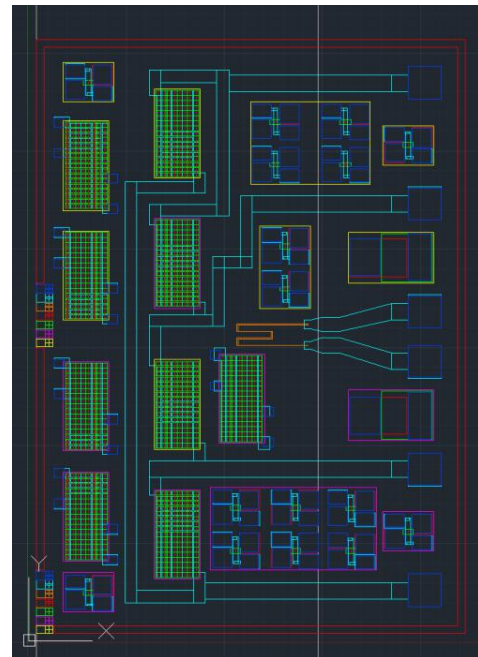
Sample: TJ2063/68

- 1) Vapor Prime 30 min (Recipe - 0):
- 2) Coat 1.5 μm PR (Recipe 6/2)
- 3) Lithography – Machine: DWL

MAP: CSNEW                      Mask: csl6 (inverted)  
Energy: 75 %                      Power: 100 mW  
Focus: 0                              Origin: (268;154) μm

- 4) Development (Recipe 6/2)

**Observations:**



➤ **Step 21: Final passivation - deposition of alumina (Al<sub>2</sub>O<sub>3</sub>)**

Sample: TJ2063/68

Machine: UHV2

BP: 1.4x10<sup>-6</sup>



Expected thickness: 1500 Å

	Deposition Time	Al <sub>2</sub> O <sub>3</sub> thickness	Ar gas flow	Pressure	Power Source	Frequency (Hz)
Read	2h		45 sccm	2 mTorr	200 W	545

➤ **Step 22: Lift-off Alumina**

Sample: TJ2063/68

- 1) Hot Micro-Strip (65°C) + Ultrasounds
- 2) Rinse with IPA + DI water + dry compressed air

**Observations:**

➤ **Step 23: Dicing Saw**

Sample: TJ2063/68

For automatic cut use:

Channel x : 5.63 mm

Channel y: 7.60 mm



## **Appendix B**

# **Radiation test plan**

# Radiation Test Plan

## Contents

1	Introduction .....	2	2.2.3	SV (Component C).....	5
1.1	Scope.....	2	2.3	Radiation test and characterisation facilities.....	5
1.2	General.....	2	2.3.1	Co-60 irradiation at HDR....	6
1.3	Purpose .....	2	3	Test Plan.....	6
2	General Procedures and Equipment.....	2	3.1	Pre-Irradiation Tests .....	6
2.1	Components Description .....	2	3.2	Irradiation Plan .....	6
2.2	Component parameters .....	3	3.3	Annealing Plan	<b>Erro! Marcador não definido.</b>
2.2.1	MgO-based MTJ (Component A).....	3	4	Annex I - Test Plan Forms .....	7
2.2.2	AlOx-based MTJ (Component B).....	4			

## **1 Introduction**

### **1.1 Scope**

This document presents the radiation test plan which was prepared in the scope of a Master's Thesis in Engineering Physics, at Instituto Superior Técnico of Lisbon's University, entitled as "Development and assessment about radiation effects on MR sensors for space applications". This project is the result of a collaboration between INESC-MN and LIP.

### **1.2 General**

The main goal of this project is to assess what would be the behaviour of different types of magnetoresistive (MR) sensors when subjected to harsh environments as, for example, in space. For that purpose, the sensors will be irradiated with gamma radiation resultant from the decay of Co-60 source. The irradiation will proceed up to a pre-defined level of interest in order to evaluate the total ionization dose (TID) effects. Three types of MR sensors will be irradiated at high rate doses (HRD). Afterwards, the results will be compared in order to understand if it would be favourable to use these sensors on devices for space applications.

The type of elements under evaluation will be firstly presented. Then the irradiation's procedure is defined.

### **1.3 Purpose**

The purpose of this document is essentially to give the essential information (characteristics and specifications) about the selected magnetic sensors, and define a radiation test plan in order to know how these will be irradiated, and try to understand how much resistant these sensors are to radiation, i.e., what are the levels of ionizing dose that the components are able to support.

## **2 General Procedures and Equipment**

### **2.1 Components Description**

The test plan consists on the evaluation of three types of magnetic sensors all manufactured at INESC-MN. The sensors are identified in the following Table.

Table 1 - List of MR sensors to be evaluated

Component type		Component		N. of units
		Sample ID	Manufacturer	
A	MgO-based MTJ	TJ937	INESC-MN	9
B	AlOx-based MTJ	TJ2063/68	INESC-MN	5
C	SV	36SV2845	INESC-MN	7

## 2.2 Component parameters

For these components, the relevant parameters to measure are: resistance, MR signal, coercivity field, transfer curve offset, voltage output, and offset voltage. These parameters are evaluated before, after each step of irradiation, and at least two times after the irradiation. The main goal of these characterisations consists on gathering enough data in order to verify if the behaviour of the sensors remain unchanged (between sensors of the same component) after irradiation, and also to conclude if there is any significant variation among them. All of the components will be unbiased during the irradiations, and characterised, at INESC-MN, under bias conditions.

### 2.2.1 MgO-based MTJ (Component A)

Component A is a MR sensor employing tunnel effect through an insulator barrier of MgO (Sample ID: TJ937). Each sensor consists on 26 magnetic tunnel junctions (MTJs) connected in series, as presented in the Figure 1. Each pillar junction has an area of  $100 \times 100 \mu\text{m}^2$  and a characteristic resistance area product of  $40 \text{ k}\Omega\mu\text{m}^2$ . The MTJ stack from the bottom to the top is the following:

Si / SiO<sub>2</sub> 10000 / Ta 50 / Ru 150 / Ta 50 / Ru 150 / Ta 50 / Ru 50 / IrMn 200 / CoFe<sub>30</sub> 20 / Ru 8.5 / CoFe<sub>40</sub>B<sub>20</sub> 26 / MgO 10 / CoFe<sub>40</sub>B<sub>20</sub> 20 / Ta 2.1 / NiFe 40 / Ru 2 / IrMn 60 / Ru 20 / Ta 50 / Ru 100 / TiWN<sub>2</sub> 150

“element” “thickness (in angstroms)”.

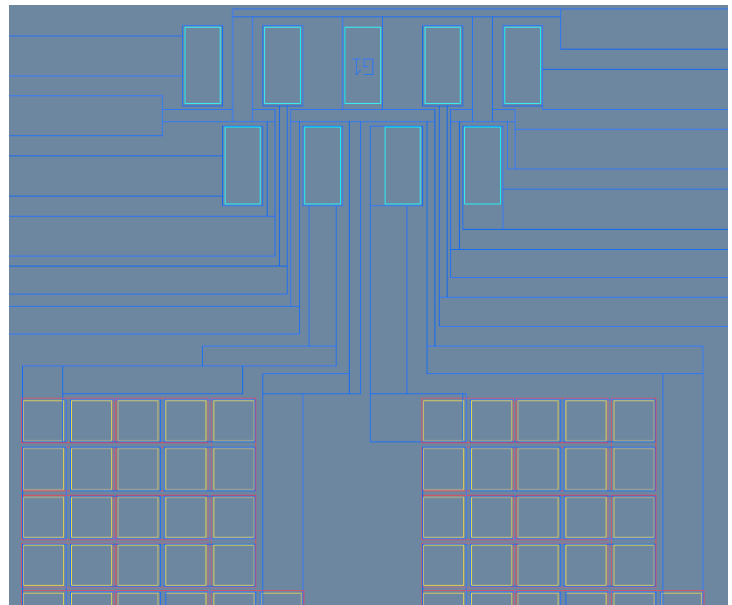


Figure 1- Two MR sensors composed by series of 26 MgO-based MTJs.

Top contacts in blue, bottom contacts in red, MTJ pillar in brown, and pads in cyan. MTJ pillar dimensions:  $100 \times 100 \mu\text{m}^2$

For the characterisations, these components are biased with a current,  $I_{bias} = 1,5 \text{ mA}$  (corresponding a drop voltage of  $\sim 6,5 \text{ mV}$  per junction; for more than  $\sim 10 \text{ mV}$  per junction the signal starts to decrease).

The parameters listed on Table 2 shall be measured prior to irradiation, between irradiation steps, and after irradiation finished.

**Table 2 - Electrical parameters to be assessed for component A**

Parameters	Symbols	Test Conditions	Measure Values	
			Value	Un.
Resistance	R	$I_{bias} = 1,5 \text{ mA}$		$\Omega$
MR ratio	MR			-
Coercivity field	$H_c$			Oe
Curve offset	$H_r$			Oe
Sensitivity	S			$\Omega/Oe$

## 2.2.2 AlOx-based MTJ (Component B)

This component also consists in a magnetic tunnel junction sensor, but now with an insulating barrier of AlOx (TJ2063/68). The stack of the sensor is the following: Ta 50 / [Ru 150/ Ta50]x3 / NiFe 30 / CoFeB 30 / Al 8 (Ox 30") / CoFeB 30/ Ru 6 / NiFe 30 / MnIr 180 / Ru 150 / Ta 50 (thickness in angstroms).

The main purpose of these sensors were to develop and test a full Wheatstone bridge (WB) for irradiation. The WB are formed by 4 resistors each one constituted by 136 MTJs in series, observed in Figure 2 (top). Each junction has an area of  $2 \times 40 \mu\text{m}^2$ . The bridges will be biased with a voltage of  $V_{bias} = 1,5 \text{ V}$ . The parameters

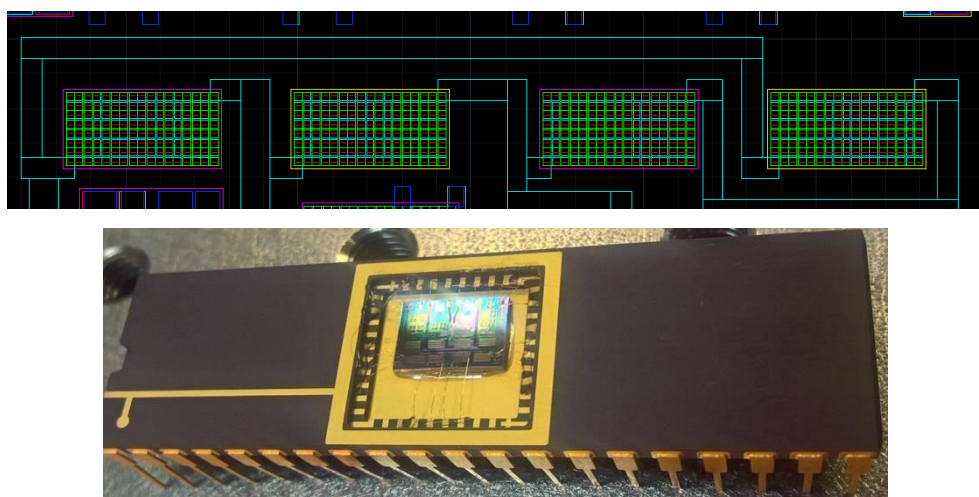


**Figure 2 – (top) Full Wheatstone bridge configuration; (bottom) Chip implemented on a chip-carrier.**

listed in Table 3 shall be measured prior to irradiation, in between radiation steps, and after radiation finishes.

Table 3 - Electrical parameters to be assessed for component B (full Wheatstone bridge).

Parameters	Symbols	Test Conditions	Measure Values	
			Value	Un.
Voltage output	$V_o$	$V_{bias} = 1,5 V$		V
Voltage offset	$V_o(H=0)$			V
Bridge resistance	$R_{bridge}$			$\Omega$
Coercivity field	$H_c$			Oe
Curve offset	$H_f$			Oe
Sensitivity	S			mV/Oe

### 2.2.3 SV (Component C)

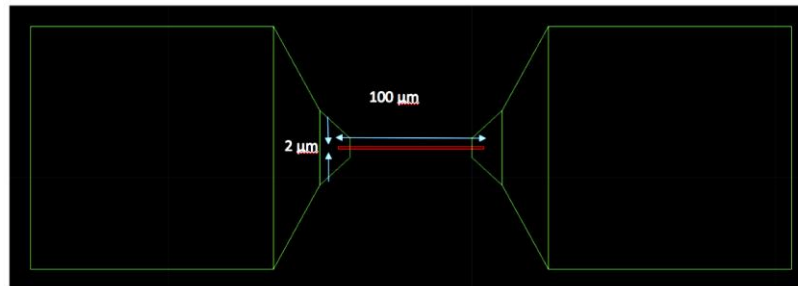


Figure 3 – SV structure and respective dimensions. It is possible to identify the pads where the probes to measure the signal are placed (green squares), and the magnetic element itself (red).

Component D, presented in Figure 4, is a spin-valve structure (Sample ID: 36SV2845), and has the following stack: NiFeCr 50 / NiFe 28 / CoFe 22 / Cu 22 / CoFe30 / Ru 8 / CoFe 26 / NiFe 7 / MnNi 300 / NiFeCr 90 , thickness in angstroms. The sensing area has dimensions of  $100 \mu m^2$ .

This component will be characterised with a bias current of  $I_{bias} = 1 \text{ mA}$ , and again, the following parameters listed in Table 4 shall be measured for the same phases as before mentioned.

Table 4 – Some of the electrical parameters to be assessed for component C

Characteristic	Symbols	Test Conditions	Measure Values	
			Value	Un.
Resistance	R	$I_{bias} = 1 \text{ mA}$		R
MR ratio	MR			-
Coercivity field	$H_c$			Oe
Curve shift	$H_f$			Oe
Sensitivity	S			$\Omega/Oe$

## 2.3 Radiation test and characterisation facilities

During two days, the irradiation tests will occur in a Portuguese facility, CTN-IST (Campus Tecnológico e Nuclear – Instituto Superior Técnico), at the Technological Unit of Radiosterilization (UTR). After each step of irradiation, the measurements will be done, in a remote facility, at INESC-MN.

### 2.3.1 Co-60 irradiation at HDR

The components will be irradiated using a Cobalt-60 radioactive source up to a level of interest dose of ~ 5 MRad at a high dose rate 1.688 MRad/hour. The dosimetry system of the facility should provide information about the absolute dose of the device under test with a resolution better than 10% and the dose rate of the Cobalt-60 source, should be known up to 5% level or better.

## 3 Test Plan

### 3.1 Pre-Irradiation characterisations

A pre-irradiation test phase is foreseen in the present plan. The aim of this phase is to prepare the to acquire pre-irradiation data (characterisations before irradiation) about components for later comparison with the data to be acquired during the irradiation and after it. These characterisations were done at INESC-MN.

### 3.2 Irradiation Plan

The irradiation test plan foresees the irradiation of the test components in several conditions. About 9, 5, and 7 sensors of MgO and AlOx - based MTJ, and SV, respectively, are implemented on chip-carriers (Figure 4). This implementation allows an easier manipulation of the devices and also a faster characterisation of the sensors once irradiated.

The chip-carriers will allow two modes of operation: Measurement and irradiation. In the irradiation mode the samples will be unbiased. In the measurement mode, the carrier-chip will couple to an adequate measuring system in order to evaluate the magneto-transport properties. After irradiations, more measurements will be done: one, two, and 30 days after it.

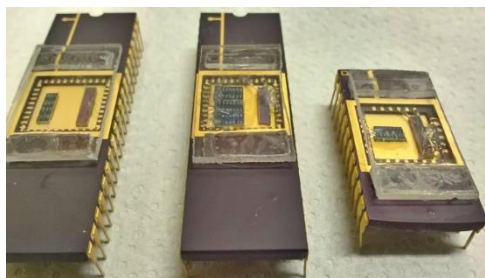


Figure 4 – Chip-carrier with the SV and MgO-based MTJs sensors.

## 4 Annex I - Test Plan Forms

### Specifics for Co source

Test facility name and address.	IST – CTN, Loures, Portugal
Name of facility and type of radiation source.	IST – CTN Co-60
Type of exposure (single or multiple).	Multiple irradiation
Level of Interest.	5 Mrad
Multiple exposure: specification of number of exposures, doses and dose rates (or flux and duration of each exposure).	(see table below)
Irradiation test sequence	(see table below)

21: Multiple exposure: specification of number of exposures, doses and dose rates (or flux and duration of each exposure).

Multiple Irradiation Steps	1	2	3
Dose(Mrad(Si))	1.688	3.376	5.064
Dose Rate (Mrad(Si)h <sup>-1</sup> )	~1.688	~1.688	~1.688
Exposure Time	~60min	~60min	~60min

25: Irradiation test sequence 1

Test Step	Description	Observations
1	Irradiation T0 -> T0 + 60min	1 hour irradiation
2	Measurement @ T0 + 85min	25 min travel + 1 hour measurement
3	Irradiation T0+170min -> T0+230min	25 min travel -> 1 hour irradiation
4	Measurement @ T0+255min	25 min travel + 1 hour measurement
5	Irradiation T0+340min -> T0+400min	25 min travel -> 1 hour irradiation
6	Measurement @ T0+425min	25 min travel

### Specifics for Component A

Component designation.	TJ937
Manufacturer's name and address.	INESC-MN
Irradiation conditions: remote or in situ, biased or unbiased.	Unbiased; (Remote characterisations)
Electrical parameters to be tested	Table 1

## Specifics for Component B

Component designation.	TJ2063/68
Manufacturer's name and address.	INESC-MN
Irradiation conditions: remote or in situ, biased or unbiased.	Unbiased; (Remote characterisations)
Electrical parameters to be tested	Table 3

## Specifics for Component C

Component designation.	36SV2845
Manufacturer's name and address.	INESC-MN
Irradiation conditions: remote or in situ, biased or unbiased.	Unbiased; (Remote characterisations)
Electrical parameters to be tested	Table 4